Science Advances
AAAS

Supplementary Materials for

Subarctic climate for the earliest *Homo sapiens* in Europe

Sarah Pederzani*, Kate Britton, Vera Aldeias, Nicolas Bourgon, Helen Fewlass, Tobias Lauer, Shannon P. McPherron, Zeljko Rezek, Nikolay Sirakov, Geoff M. Smith, Rosen Spasov, N.-Han Tran, Tsenka Tsanova, Jean-Jacques Hublin

*Corresponding author. Email: sarah_pederzani@eva.mpg.de

Published 22 September 2021, *Sci. Adv.* **7**, eabi4642 (2021)
DOI: 10.1126/sciadv.abi4642

This PDF file includes:

Supplementary Texts S1 to S10
Figs. S1 to S13
Tables S1 to S3
References

Supplementary Text

S1. Stratigraphy and chronology of Bacho Kiro Cave

Bacho Kiro Cave is located in north-central Bulgaria in the town of Dryanovo, Gabrovo province (Fig. 1). The cave site was originally excavated by Dorothy Garrod in 1938 (*44*) and re-excavated by B. Ginter and J. K. Kozlowski from 1971-1975 (*10*) and more recently, since 2015 by a joint team from the Bulgarian National Archaeological Institute with Museum (NAIM-BAS, Sofia) and the Department of Human Evolution, Max-Planck-Institute for Evolutionary Anthropology, Leipzig, Germany (MPI-EVA). The archaeological sequence of the cave encompasses the late Middle Palaeolithic (Layer N1-K) through the early Upper Palaeolithic, with notable Initial Upper Palaeolithic units (here Layers N1-I & I and N1-J & J, originally Layers 11 and 11a) originally termed 'Bachokirian' (Fig. S2).

Two excavation sectors were opened in the most recent excavation, the Main Sector and an additional sector in a side chamber, termed Niche 1. Layer terminology designates units in Niche 1 with the prefix "N1-." The deposits in the two sectors are not physically connected, as between them the stratigraphic sequence has been removed by previous excavations, but archaeological layers in the lower portion of the sequence can be correlated based on archaeological and geological observations (Fig. S2) (*5*). Based on these observations, Layers N1-H/G, N1-I and N1-J in Niche 1 clearly correspond to Layers G, I and J in the Main sector (*5*). This is also supported by good agreement of the ^{14}C dates of N1-I & I and N1-J & J (*6*). For this reason we group samples from Layer I and N1-I in a single archaeological unit in this study that we designate as N1-I & I. Samples from the contact between two layers are grouped separately and labelled accordingly, for example as N1-I/J.

The upper part of the sequence consists of a number of uncorrelated Upper Palaeolithic layers (C, B, A2 and A1 in the Main Sector and N1-3a and N1-3b in the Niche) followed by layers with undiagnostic lithic assemblages (D through F and N1-3c through N1-3e) (*5*). Immediately above the most prominent Initial Upper Palaeolithic layer (N1-I & I) sits a unit of essentially archaeologically sterile Layers N1-H/G and G, which are characterised by laminated sediments indicating a rapidly accumulated water deposition (*5*). The contact between Layer N1-I & I and the overlying layers is sharp and erosive. artefacts occur very rarely in Layers N1-G & G and N1-H and only in the lowermost portion. They appear to to be reworked material from the surface of Layer N1-I & I (*5*). We therefore consider material from the contact of Layer N1-H and N1-I as belonging to the IUP Layer N1-I & I complex and group them as such.

Contact between Layer N1-J and the underlying Middle Palaeolithic Layer N1-K is gradual and was difficult to pinpoint during excavations. Additionally, Middle Palaeolithic artefacts made from coarse grained raw material (analogous to the majority of the artefacts from Layer N1-K) have been recovered from the lower portion of Layer N1-J. Radiocarbon dates from Layer N1-J show three distinct age clusters (radiocarbon dates reported in ref. (*6*) have been recalibrated here using the IntCal20 calibration curve (*7*) in OxCal v4.4(*45*)). In the lower part of Layer N1-J, two bones yielded ages > 51,000 BP and a second cluster of dates ranged from 48,130 - 46,030 cal BP (modelled age, 94.5% probability). In terms of artefacts, these lower portions of N1-J cannot be securely associated with either the IUP or the underlying MP. The middle and upper portion of Layer N1-J dates from 45,990 - 44,540 cal BP (modelled age, 94.5% probability) and is associated with IUP artefacts that are technologically consistent with the lithic record in the overlying Layer N1-I. The Layer J dates from the Main Sector are consistent with the youngest of these age clusters (44,990 - 44,020 cal BP modelled age, 94.5% probability). Combined with field observations and micromorphological indicators these dates support the conclusion that only the upper portion of the Layer N1-J & J complex is preserved in the Main Sector. The radiocarbon dates for Layer N1-J & J and N1-I & I, the techno-typological characteristics, and the increase in artefact density from N1-J & J to N1-I & I support the interpretation that the IUP occupation began during the formation of Layer N1-J & J and intensified in Layer N1-I & I, representing a relatively continuous human presence in the cave. This places the beginning of the IUP at Bacho Kiro most likely around 45,990 cal BP (95.4% probability).

The Middle Palaeolithic Layer (N1-K) forms the base of the stratigraphic sequence in the cave, but in the new excavations is only present in the Niche 1 sector. All five radiocarbon dates from this layer are older than 51,000 BP (beyond the radiocarbon range) (*6*). OSL dates on the fine grain fraction from Layer N1-K have so far yielded an age 61 $\pm$ 6 ka (see Supplementary Text S2). As the geological observations in the cave suggest that the Layer K sediments originate from further inside the cave, sediments are likely to have been recycled to some extent inside the cave and the OSL dates should therefore be regarded as a maximum age. This means that the age of Layer N1-K is constrained between this date of 61 $\pm$ 6 ka and the ^{14}C dates of > 51,000 BP. These dates place the Middle Palaeolithic at Bacho Kiro as most likely falling into early MIS 3 or possibly late MIS 4.

S2. Luminescence dating

To obtain chronological information on the depositional age of Layer N1-K, optically stimulated luminescence was applied to the 4-11 microns polymineral fraction. This layer extends beyond the range of the radiocarbon method (> 51,000 BP), but luminescence dating (*46*) provides the opportunity to cover a time range going back several 100 ka (e.g. *47*). Sample preparation was undertaken at the luminescence laboratory within the Department of Human Evolution at the Max Planck Institute for Evolutionary Anthropology in Leipzig (MPI-EVA). It included the common steps of chemical treatment (10 % HCL; sodium oxalate and 15 % H_2O_2) and centrifuging. Luminescence measurements were conducted on a Risø TL-DA-20 reader equipped with a beta source (dose rate = 0.19 Gy/s) and IR emitting diodes (870 nm) for feldspar stimulation. For De-measurements, the $pIRIR_{290}$ approach (*48*, *49*) was used, stimulating the feldspar signal at an elevated temperature after bleaching the IR_{50} related electron traps. This signal is known to be characterized by a stable luminescence emission (*50*) and mostly avoids the correction for anomalous fading. The latter would lead to an age underestimation if not accounted for properly (*51*). The luminescence signal was recorded using a D410 filter allowing to detect the blue-violet emission. Prior to the De-measurements, the protocol was tested for its reproducibility using a dose recovery test, which successfully recovered the given dose with a ratio of 1.03 $\pm$ 0.02. As quality criteria, only aliquots showing a recycling ratio deviation < 10 % from unity and a recuperation value < 5 % were accepted. Fading measurements were applied for 6 aliquots and the $pIRIR_{290}$-related g-values was at 1.3 ± 0.2 highlighting that fading has only a negligible effect for sampled material from Bacho Kiro. Calculating an age using luminescence dating also requires the evaluation of the dose rate mainly defined by the activity of ^{238}U, ^{232}Th and ^{40}K within the sediment-unit of interest. Therefore, high resolution gamma spectrometry was applied at the Felsenkeller laboratory (VKTA) in Dresden. The obtained nuclide concentrations are listed in Table S1. A water content of 16 $\pm$ 10 % was used to account for dose rate attenuation by moisture. The high error was chosen with respect to significant potential fluctuations of the moisture in Layer N1-K over the relevant geological time-scale. To consider the alpha efficiency, an a-value of 0.086 $\pm$ 0.004 was used (*52*). The $pIRIR_{290}$ luminescence age estimate obtained from Layer N1-K points to a deposition of the sediments at 61 $\pm$ 6 ka. As there is indication for sediment reworking inside the cave system, this age should be interpreted as a maximum age. Nevertheless, a significant age overestimation can be excluded keeping in mind the radiocarbon-chronology from the capping units (see Supplementary Text S1).

S3. Faunal assemblage

Bone surface modifications

The relative frequency of human modifications of bone fragments compared to modifications made by carnivores gives an indication of the origin and formation process of the Bacho Kiro Cave faunal assemblage. In the IUP Layer N1-I & I as well as at the contact between N1-I and N1-J/J and I (grouped as N1-I/J & I/J), human modifications clearly dominate the modified bone fragments, with very few carnivore marks present (Fig. S3). In Layer N1-J & J carnivore modifications become more frequent, occurring at the same frequency as human modifications throughout this layer. This suggests that the IUP faunal assemblage, particularly in Layer N1-I & I and the contact to Layer N1-J & J is of anthropogenic origin. This means that the stable isotope results generated in this study can be directly tied to environmental conditions that persisted during human activity at Bacho Kiro Cave. However, for the main part Layer N1-J & J (except the contact with Layer N1-I & I), the contact between N1-J and N1-K (N1-J/K), as well as Layer N1-K, this is no longer securely the case. Carnivore modifications in these units occur with the same or higher frequency than human modifications and it therefore cannot be clearly determined if faunal remains from these layers originate from prey of humans or carnivores. The stable isotope results from these layers are therefore not necessarily specifically tied to the time of human occupation of the cave, but have to be interpreted as generally representative of the time of layer formation, which occurred between 61 $\pm$ 6 ka ago and 51 ka BP (infinite radiocarbon age).

Season of death

As temperatures fluctuate seasonally the seasonality of site use can be a key factor in our understanding of the climatic conditions that humans experienced at an archaeological site. In the case of Bacho Kiro Cave, oxygen isotope analysis of equid and *Bos/Bison* tooth enamel shows that, despite very low mean annual and winter temperatures, summer temperatures were still reasonably high, particularly in Layer N1-J and the contact between N1-J and N1-I (N1-I/J). It is therefore of particular interest, whether humans were present at the site also during the colder parts of the year. Information on seasonality of site use can be obtained by determining the season of death of human prey animals based on age data from epiphyseal fusion and tooth development and wear. The analysis of season of death for the Bacho Kiro Cave faunal assemblage is still ongoing, but preliminary pilot data from a small number of equid, *Bos/Bison*, and bear individuals suggest that at least some animals were hunted during the colder parts of the year. Ursids are included, as bear remains from the cave (particularly in Layer N1-I & I) commonly exhibit butchery marks, indicating that they were hunted by humans (*5*). In the IUP

layers (N1-I & I and N1-J & J) seasons of death include spring (equid dP4, *Bos/Bison* M2 tooth wear), spring/summer (equid dI2), autumn/winter (2 unfused equid phalanges), winter (ursid canine tooth wear) and winter/spring (Ursid M1 germs). In Layer N1-K the tooth wear of a *Bos/Bison* M2 suggests death during the winter, although it should be noted that the faunal assemblage of this layer constitutes a mixture of anthropogenic and carnivore deposition. These data suggest that for the IUP there was at least some human presence at Bacho Kiro Cave during the colder parts of the year, despite the low temperatures reconstructed for these seasons. Given the limited nature of the season of death data, however, it is currently not possible to say whether intensity or frequency of site use differed between seasons.

S4. Oxygen isotopes of tooth enamel as a palaeotemperature proxy

Oxygen isotope delta values ($\delta^{18}O$) of bioapatite - the mineral portion of teeth and bones - of obligate drinking terrestrial animals can be used to reconstruct past air temperatures. This is based on two relationships that together form the basis of bioapatite $\delta^{18}O$ as a temperature proxy. 1) There exists a strong linear relationship between temperature and $\delta^{18}O$ in precipitation ($\delta^{18}O_{precip}$) and most surface water in mid- to high latitudes (*53–58*), where low $\delta^{18}O$ correspond to low temperatures and high $\delta^{18}O$ values represent higher temperatures. 2) Animals that regularly drink large amounts of open water (such as aurochs/bison, horses or mammoths) record the oxygen isotopic composition of surface water that they consume in the oxygen isotopic composition of tooth and bone bioapatite (*59–62*). In combination, these two effects enable the reconstruction of palaeotemperatures using faunal skeletal remains. In this study we specifically use the oxygen isotope composition of tooth enamel bioapatite phosphate ($\delta^{18}O_{phos}$), which is most resistant to diagenetic changes.

Oxygen isotope delta values can be compared directly between layers or groups to draw inferences on relative changes in seasonality (summer to winter differences) or temperature (warmer vs colder, more seasonal vs less seasonal). However, for comparisons of different species or with other climatic proxies, a conversion to reconstructed drinking water $\delta^{18}O$ ($\delta^{18}O_{dw}$) or temperature is necessary (see Supplementary Text S8). This conversion to palaeotemperatures relies on formalised versions of the linear relationships between temperature and $\delta^{18}O_{precip}$, as well as between $\delta^{18}O_{dw}$ and $\delta^{18}O_{enamel}$ (*15*, *37*, *60*, *61*, *63–66*).

While the temperature effect on $\delta^{18}O_{precip}$ is pronounced in mid- to high latitudes, other effects can impact $\delta^{18}O_{precip}$ and $\delta^{18}O_{enamel}$ (*67*). This means that assumptions of the palaeotemperature proxy model have to be tested and potential interfering effects have to be reasonably excluded in

each study-setting to confirm the use of $\delta^{18}O$ as a temperature proxy. Firstly, the use as a temperature proxy relies on the assumption that studied animals drink relatively large amounts of water and that this water generally reflects $\delta^{18}O_{precip}$. Large Bovidae such as cattle or Bison as well as equids such as horses are obligate drinkers and have a very limited ability to meet a substantial portion of their large water requirements from other sources such as water contained in food (*68–75*). In modern-day settings these taxa have been reported to regularly consume large quantities of drinking water across diverse environmental settings (*68–71*, *73*, *75*) and their $\delta^{18}O_{enamel}$ has consequently been shown to be strongly tied to $\delta^{18}O$ of local precipitation (*65*, *76–80*). Considering the metabolic constraints on water requirements and the lack of variability in drinking behaviour across modern ecosystems in these taxa, we feel that it is reasonable to assume a similar drinking behaviour in the Upper Pleistocene.

The second fundamental assumption regarding the relationship between $\delta^{18}O_{dw}$ and $\delta^{18}O_{precip}$ is necessary, as the relationship between temperature and $\delta^{18}O$ is established using modern measurements of $\delta^{18}O_{precip}$. And indeed, most open water sources relatively closely reflect $\delta^{18}O_{precip}$ (*81*). However, this is not the case for all water bodies, and therefore regionally available water sources in the study region need to be examined with this in mind. Water sources that commonly can be significantly isotopically decoupled from local precipitation are deep groundwaters, large rivers, and large lakes, due to effects of water transport, water residence time and evaporation (*82–84*). Substantial water consumption from highly evaporated lakes would cause animals to exhibit high $\delta^{18}O_{enamel}$ values, which is in contrast to the uncommonly low oxygen isotope values of the animals from Bacho Kiro Cave measured in this study. Combined with the absence of large lakes in the vicinity of the site, substantial consumption of evaporated lake water is unlikely. This leaves the possibility of river or groundwater consumption. Bacho Kiro Cave is located at 335 m a.s.l. and is situated directly above the small stream of the Andaka river, which flows into the Dryanovo river (also called the Dryanovska river) in immediate proximity to the cave. Both rivers are relatively small, and therefore are most likely isotopically representative of local precipitation in the catchment with relatively little potential for strong buffering or time averaging effects (*82*, *83*). In the absence of isotopic measurements from these rivers, we can therefore use precipitation oxygen isotope delta values to estimate how strongly these rivers are likely to isotopically deviate from precipitation in the vicinity of Bacho Kiro Cave. The Dryanovo river originates at 980 m a.s.l. and flows into the Belitsa river close to the town of Debelets, approximately 25 km northeast of Bacho Kiro Cave (*85*). The drainage basin has an average elevation of 667 m a.s.l.(*86*) The estimated $\delta^{18}O_{precip}$ value for the Dryanovo river origin is -10.6 $\pm$ 0.4 ‰, ranging from -14.7 ‰ in winter to -4.9 ‰ in summer (*87*). Local precipitation at Bacho

Kiro Cave is estimated to have a $\delta^{18}O_{precip}$ of -9.0 $\pm$ 0.3 ‰, ranging from -13.2 ‰ in winter to -3.9 ‰ in summer (*87*). This means that an oxygen isotopic difference of no more than approximately 1 - 1.5 ‰ is expected between local precipitation at Bacho Kiro Cave and the river water of the Dryanovo river. Animals drinking mostly from the Dryanovo river would have artificially slightly lowered $\delta^{18}O_{enamel}$ values, leading to a slight underestimation of palaeotemperatures. However, this temperature underestimation would at most only be approximately 2.5 °C, which falls within the range of uncertainty of the palaeotemperature reconstructions made in this study. For the Initial Upper Palaeolithic layers, raising the palaeotemperature estimates by 2.5 °C would still result in temperature estimates that are consistent with a pronounced cold phase. The larger Yantra river could also potentially have served as a water source, flowing ~ 10 km west of Bacho Kiro Cave. $\delta^{18}O_{precip}$ at the source of the Yantra river is estimated to be -11.4 $\pm$ 0.5 ‰, 2.4 ‰ lower than precipitation at Bacho Kiro Cave (*87*). This would mean a slightly larger maximum possible temperature bias of ~ 5 °C. Nonetheless, elevating the reconstructed temperatures by this amount would result in reconstructions that still fall within the temperature variability of Upper Pleistocene cold phases (*22*). Additionally, it should be considered that this constitutes an estimate of maximum possible isotopic difference between the river and local precipitation at Bacho Kiro Cave. Given that precipitation from the complete catchment up to the Dryanovo area - which has an average elevation of 545 m a.s.l.(*86*) - contributes to the river water, the actual isotopic difference to local Dryanovo precipitation is most likely significantly smaller. It should also be noted that, given the larger size of the Yantra river and the spring and summer contribution from snowmelt to this river (*86*), animals drinking from this river would be expected to show a significantly reduced seasonal amplitude in $\delta^{18}O$, which is not the case (see Supplementary Text S6). Another drinking water source that could result in artificially lowered temperature reconstructions would be springs fed from old groundwater, formed during a colder time period. However, such groundwaters have by definition a very long residence time, and are seasonally completely or almost completely invariable (*82*, *88–90*). Animals regularly consuming such spring water would therefore also be expected to show no seasonal sinusoidal $\delta^{18}O$ curves, which is not the case in this study. This makes a bias on temperature reconstructions from groundwater consumption unlikely. We therefore conclude that animals using precipitation-decoupled drinking water sources is either unlikely in some cases or of negligible isotopic magnitude in other cases and would not change the conclusions made in this study, supporting the use of $\delta^{18}O_{enamel}$ as a temperature proxy.

An additional consideration in the use of $\delta^{18}O_{enamel}$ to obtain palaeotemperature estimates is the variability in the exact relationship between $\delta^{18}O_{precip}$ and air temperature. For

palaeotemperature reconstruction, this relationship is established using modern-day calibration data (see methods in Supplementary Text S8) under the assumption that this relationship remains sufficiently stable throughout the archaeological time scales that are considered. However, some variability in the $\delta^{18}O_{precip}$ - air temperature relationship is known to be caused by differences in atmospheric circulation and is, for instance, visible in modern measurements as variability depending on geographic location (*81*, *91*, *92*). This means that air temperature reconstruction therefore needs to assume a certain degree of equivalency in atmospheric circulation between modern-day calibration data sets and past environments. Modern-day spatial variations in this relationship are relatively minor and the slopes of $\delta^{18}O_{precip}$-temperature regressions are overall spatially relatively robust (*58*, *81*, *91–94*), indicating that the $\delta^{18}O_{precip}$-temperature relationship is stable under moderate circulation changes. Pleistocene data that allow the characterisation of the $\delta^{18}O_{precip}$-temperature relationship are scarce, but simulations suggest relatively limited changes in atmospheric circulation and oxygen isotope data for Pleistocene precipitation compared with temperature estimates from a variety of proxies show little variability in the isotope-temperature relationship in the Upper Pleistocene compared to modern slope estimates (*63*, *66*, *89*, *95*, *96*). For instance, $\delta^{18}O$ measurements of Pleistocene groundwaters from Switzerland indicated a $\delta^{18}O_{precip}$-temperature slope of 0.497 compared to a modern-day slope of 0.44 (*63*). The effects of variability in the $\delta^{18}O_{precip}$-temperature relationship on palaeotemperature reconstruction can also to some degree be numerically incorporated during the calculation of palaeotemperature estimates by using modern-day calibration data from a range of localities with different circulation regimes (*97*), which we have specifically done in this study (see Supplementary Text S8). We therefore conclude that the assumption that modern-day $\delta^{18}O_{precip}$-temperature relationships can be applied to the Upper Pleistocene is sufficiently met.

S5. Oxygen stable isotope extended methodology

Sequential tooth enamel samples were obtained as cut strip samples similar to methods described in ref.(*98*), by first removing a ca. 0.5 cm wide section of a tooth loph covering the complete crown height. These sections were then cleaned and the adhering dentine removed to isolate the tooth enamel using surface abrasion with a tungsten carbide burr attached to a dental drill. The resulting clean sections of tooth enamel were then sectioned into a series of ~ 1 mm wide sequential sample strips. Sample strips commonly have dimensions of 1 mm in length and 5 mm width and they incorporate the complete depth of the tooth enamel layer. Usually every third strip sample was further processed for oxygen isotope analysis, resulting in series of sequential samples with ~ 2mm gaps between samples. Each strip that was chosen for oxygen isotope

analysis was first snapped in half and the other half reserved for strontium isotope analysis. These tooth enamel strip pieces were then ground to powder using an agate mortar and pestle for further processing for oxygen stable isotope analysis.

Tooth enamel powders were converted to silver phosphate (Ag_3PO_4) for oxygen isotope measurements of bioapatite phosphate following an adapted version of the rapid precipitation procotocol developed in ref.(*30*) and modified in ref.(*31*) as described in ref.(*32*). Approximately 5 mg of tooth enamel powder of each sample were weighed into 2 mL Eppendorf microcentrifuge tubes. To digest bioapatite samples and remove calcium from the resulting solution, samples were agitated in 0.4 mL of 2 M hydrofluoric acid (HF) for 24 hours. The phosphate containing solution was isolated from calcium fluoride (CaF_2) precipitate by pipetting to a new clean microcentrifuge tube after centrifugation (12000 rpm for 5 Min). To maximise phosphate recovery the CaF_2 precipitate was washed once with 0.1 mL MilliQ ultrapure water and the wash added to the phosphate containing solution. The sample solution was then brought to neutrality as indicated by the colour change point of Bromthymolblue indicator using 25% ammonia solution (NH_4OH). 60 μL of NH_4OH were first added to each sample using an automatic pipette and each solution then slowly titrated to the colour change point (yellow to green) using individual drops of NH_4OH added with a 100 μL Hamilton Microliter fixed needle syringe (Hamilton Bonaduz AG, Switzerland). From the neutralised solutions, Ag_3PO_4 was crash precipitated by addition of 0.4 mL 2 M silver nitrate ($AgNO_3$) solution. The resulting precipitate was pelleted by centrifugation (12000 rpm for 5 Min) and the silver nitrate supernatant removed. The silver phosphate was then washed three times with MilliQ ultrapure water using centrifugation and vortex mixing steps between rinses to eliminate any silver nitrate from the sample. Silver phosphate samples were then dried over night at 50 °C and stored over desiccant until further analysis.

Oxygen isotope delta measurements of Ag_3PO_4 were conducted using a high temperature elemental analyser (TC/EA) coupled to a Delta V isotope ratio mass spectrometer via a Conflo IV interface (Thermo Fisher Scientific, Bremen, Germany) at the Max-Planck-Institute for Evolutionary Anthropology (MPI-EVA). Approximately 0.5 mg of each silver phosphate sample was weighed into cleaned silver capsules (3x4 mm, IVA Analysentechnik, Meerbusch, Germany) and introduced to the TC/EA using a Costech Zero Blank Autosampler (Costech International, Cernusco sul Naviglio, Italy). Conversion to CO was achieved using a reactor temperature of 1450 °C and gases separated using an Eurovector E11521 1.4 m x 4 mm x 6 mm stainless steel GC column with 80/100 mesh 5 Å molecular sieve packing (Eurovector Instruments & Software, Pavia, Italy) maintained at 120 °C with a carrier gas pressure of 1.3 bar. Samples were measured in triplicate,

but in rare cases individual measurements were rejected if they did not meet quality control criteria such as appropriate peak area to sample amount relationship. In such cases $\delta^{18}O$ are therefore only based on two replicates.

Oxygen isotope delta values were two-point scale normalised to the VSMOW scale using matrix matched standards calibrated to international reference materials and scale normalisation was checked using three separate quality control standards. Scale normalisation was conducted using the B2207 silver phosphate standard ($\delta^{18}O$ = 21.7 $\pm$ 0.3 ‰, 1 s.d.; Elemental Microanalysis, Okehampton, UK) and an in-house silver phosphate standard (KDHP.N, $\delta^{18}O$ = 4.2 $\pm$ 0.3 ‰, 1 s.d.). This in-house standard was obtained by equilibrating a KH_2PO_4 solution with Leipzig winter precipitation at ca. 140 °C for several days, after which the solution was neutralised using a small amount of NH_4OH and the phosphate precipitated as silver phosphate by addition of $AgNO_3$ solution. The accepted value of this in-house standard was determined by two-point calibration using B2207 and IAEA-SO-6 (barium sulphate, $\delta^{18}O$ = -11.35 $\pm$ 0.3 ‰, 1 s.d.(*33*)).

Aliquots of an in-house modern cow enamel standard (BRWE, later replaced by BRWE.2 due to exhaustion of this material) and the standard material NIST SRM 120c (formerly NBS 120c) were precipitated and measured alongside each batch of samples to ensure equal treatment. Additionally, a commercially available silver phosphate (AS337382, Sigma Aldrich, Munich, Germany) was used as a third quality control standard to check across-run consistency of scale normalisation independent of silver phosphate precipitation. Measurements of these standards gave $\delta^{18}O$ values of 14.9 $\pm$ 0.4 ‰ for BRWE (1 s.d., n = 53), 21.7 $\pm$ 0.5 ‰ for NIST SRM 120c (1 s.d., n = 37) and 13.9 $\pm$ 0.2 ‰ for AS337382 (1 s.d., n = 159). This compares well to the consensus value for NIST SRM 120c of 21.7 ‰ (*34*), as well as the long-term averages for BRWE of 15.2 $\pm$ 0.3 ‰ and for AS337382 of 14.0 $\pm$ 0.3 ‰. The BRWE.2 standard used in the later part of the study to replace the BRWE standard gave a mean of 14.3 ‰ with a between-run reproducibility of 0.3 ‰ (1 s.d., n = 17). Samples were usually measured in triplicate and average reproducibility of sample replicate measurements was 0.3 ‰. Consecutive analysis of sets of standards with widely spaced isotopic value showed no detectable memory effect and consequently no memory effect correction was used. No effect of the blank, of the sample amount, or peak height on the results was observed and consequently no blank correction or linearity correction was used. If drift across the course of a run was detected in the quality control standard AS337382, a linear drift correction based on the drift of both normalisation standards was used, and checked with the quality control standard.

S6. Oxygen isotope time series

When using tooth enamel, a time dependent series of $\delta^{18}O$ values with sub-annual resolution can be obtained by employing a serial sampling approach. As tooth enamel incrementally forms from the crown to the root and is essentially biologically inert after its formation (*99*, *100*), a series of small samples can be taken along the tooth growth axis to obtain a time dependent series of $\delta^{18}O$ measurements. This time series covers the time of tooth formation, which is usually several months to over a year in *Bos/Bison* and one year to 1.5 or 2 years in equids such as horses and donkeys, depending on the tooth type and tooth wear (*42*, *43*, *101*). In this study, for *Bos/Bison* a mixture of second (M2) and third molars (M3) were used, which - in extant bison - mineralise from the two months to 14 months of age (M2) and from 9 months to 2 years of age (M3) respectively, covering approximately one year and 1.3 years of isotopic input in their unworn state (*43*). Tooth wear can, however, substantially reduce the amount of isotopic input preserved on the remaining tooth crown, as earlier forming portions of the tooth are removed. Equid teeth used in this study are comprised of second, third and fourth premolars (P2, P3 and P4) as well as second and third molars (M2 and M3). In extant horses these teeth mineralise on average from 7 to 37 months (M2), from 13 to 31 months (P2), from 14 to 36 months (P3), from 19 - 51 months (P4) and from 21 to 55 months of age (M3)(*42*). In their unworn state these teeth consequently record between 1.5 years (P3) and nearly 3 years (M3 and P4) of isotopic input. First molars were not included, as they mineralise during consumption of mothers' milk, which impacts $\delta^{18}O$ of tooth enamel. Second molars in both *Bos/Bison* and equids can start mineralising in the late phases of nursing, however these early forming portions of the tooth are usually not preserved in worn teeth. As only teeth with a reasonable amount of wear were used in this study, an effect of nursing on our $\delta^{18}O$ results is unlikely. Indeed, the *Bos/Bison* second molars used here both preserve less than 6 months of isotopic input, while the single equid second molar (AA7-121) preserves approximately 1.5 years out of 2.5 years of total mineralisation time (Fig. S4).

Due to the seasonal temperature related variability in surface water consumed by these animals, extracted time series of $\delta^{18}O$ values commonly display a sinusoidal shape with peaks indicating the summer season and troughs the winter season (*101*, *102*). Such $\delta^{18}O_{phos}$ time series with a discernible sinusoidal shape with summer (high temperature) peaks and/or winter (low temperature) troughs are detectable for the majority of studied teeth (Fig. S4). Three *Bos/Bison* teeth (AA7-141, AA8-334 and AA7-2017) do not record a clearly visible peak or trough, due a combination of to the short amount of time preserved along the tooth and the timing of birth and tooth mineralisation. These teeth were therefore not used for further analysis of summer, winter or mean annual $\delta^{18}O_{phos}$ values or temperatures. In contrast, a number of *Equus sp.* teeth (such

as CC7-2478) record up to two complete annual cycles, enabling the extraction of several measurements for summer/winter climatic conditions. An overview of all individual $\delta^{18}O_{phos}$ measurements obtained for this study can be found in Table S2. Summer peak and winter trough values were determined by visual inspection of sinusoidal $\delta^{18}O_{phos}$ time series, and locations are marked on each curve in Fig. S4. These values were used as summer and winter $\delta^{18}O_{phos}$ values, that are shown in the main text Figure 1.

S7. Oxygen isotope inverse modelling

Oxygen isotope time series from sequentially sampled tooth enamel are necessarily impacted in their shape by a certain amount of time averaging of the $\delta^{18}O$ signal. This is due to the extended and complex nature of enamel formation where mineral, and therefore isotopic, input is added at several stages that mostly leave no visible incremental tissue structures that could be discretely sampled. Therefore, the sampling geometry cannot capture discrete time periods of isotopic input and thus homogenises a certain amount of isotopic input into the same sample. This means that a sample series is a significantly time-averaged representation of the original isotopic input into animal tooth enamel (*59*, *103–108*). This results in a predictable decrease of the amplitude (damping) and an offset in the position of peaks and troughs of the sinusoidal $\delta^{18}O$ curve recorded in each tooth, which needs to be corrected before faithful absolute seasonal temperatures can be reconstructed (*38*, *106–111*). If a consistent sampling strategy is used, a correction is not necessary for a relative comparison within the same species (and ideally the same tooth type), as the amount of time-averaging is approximately consistent between all studied teeth.

To correct for this damping effect on the amplitude of intratooth $\delta^{18}O$ profiles, an inverse modelling procedure using an adapted version of code published in ref.(*38*) was employed to reconstruct the original $\delta^{18}O$ input time series. This approach estimates the original $\delta^{18}O$ input into tooth enamel by inverse modelling the time-averaging introduced through the sampling procedure by taking into account the sampling geometry and species-specific parameters of enamel formation. A detailed description of the modelling procedure with associated code can be found in ref.(*38*) It should be noted that this inverse model was originally developed for ever-growing teeth and does not take into account the slowing of enamel growth towards the enamel-root-junction (ERJ) seen in some molars of large ungulates, particularly horses (*109*, *112*). However, while such considerations have been used to develop updated inverse models for sheep (*110*), no such model is currently available for horses or cattle/bison and several of the

fundamental enamel mineralisation parameters necessary for such a model are unknown for these species. For horse molars but not premolars, a model has been developed to adjust $\delta^{18}O$ profiles for the x-axis shifts caused by the slowing of tooth growth (*109*), but this model does not include any adjustments to the $\delta^{18}O$ amplitude. As we sampled a number of premolars in this study, we did not employ this model here. Due to all these factors, the amplitudes of $\delta^{18}O$ input that are reconstructed here likely represent minimum amplitudes, particularly for horse samples.

Enamel formation input parameters were chosen to reflect *Bos/Bison* or *Equus caballus* amelogenesis following values given in ref.(*107*), ref.(*106*) and ref.(*103*). For *Bos/Bison*, initial mineral content of enamel was set at 25% , enamel appositional length as 1.5 mm, and maturation length as 25 mm. For *Equus sp.* initial mineral content of enamel was set to 22%, enamel appositional length as 6 mm, and maturation length as 28 mm. Additionally, sample input variables were given for distance between samples and sample depth. During the modelling procedure a damping factor describing the damping of the isotopic profile amplitude needs to be chosen using an adjustment of a measured error term (E_{meas}) to the prediction error (E_{pred}). The adjusted damping factors determined for the specimens analysed here fell between 0.01 and 0.11. Graphical representations of the modelled $\delta^{18}O$ input time series can be found in Fig. S13.

The most likely model solutions were used to extract corrected summer peak and winter trough $\delta^{18}O$ values. Modelled summer and winter values were extracted in the $\delta^{18}O$ profile locations that correspond to peaks and troughs in the original unmodelled $\delta^{18}O$ profile. This was done to avoid using abrupt spikes, or artificially added ‘peaks’ and ‘troughs’ in $\delta^{18}O$ profiles that did not originally show a clear seasonal peak or trough. Such model artefacts can be produced in $\delta^{18}O$ profiles that do not have a sinusoidal shape, as the model presupposes a sinus curve shape (*38*). The extracted modelled summer peak and winter trough values were used as the input to generate summer and winter $\delta^{18}O_{dw}$ values as well as summer and winter absolute temperatures (see Supplementary Text 8). Mean annual $\delta^{18}O$ values were computed directly from raw $\delta^{18}O_{phos}$ values rather than from model corrected curves. If a systematic sampling geometry is applied, the inverse model essentially symmetrically extends the amplitude of the sinusoidal $\delta^{18}O$ curve, making little changes to the average $\delta^{18}O$ of an annual cycle. We therefore use annual averages from $\delta^{18}O_{phos}$ values directly to avoid the impact of uncertainty on the model output inflating the error ranges on $\delta^{18}O_{dw}$ and palaeotemperature estimates. A detailed comparison of modelled and unmodelled annual averages can be found in Supplementary Text S8.

S8. Methods for the conversion to drinking water $\delta^{18}O$ and air temperature

While raw $\delta^{18}O_{phos}$ values of individuals from different layers can be used to examine temperature change through time in a relative manner, a conversion to oxygen isotope values of drinking water ($\delta^{18}O_{dw}$) and/or absolute temperatures is necessary to compare results from different taxa or with different types of palaeotemperature records and modern-day climates. At the same time we use conversions to $\delta^{18}O_{dw}$ to assess whether the two taxa analysed in this study (aurochs/bison and *Equus sp.*) yield comparable oxygen isotope results. The assumptions and prerequisites for using faunal enamel oxygen isotope delta values as a temperature proxy are discussed in Supplementary Text S4.

The conversion to $\delta^{18}O_{dw}$ and air temperature relies on the empirically defined linear relationships between temperature and precipitation $\delta^{18}O$ ($\delta^{18}O_{precip}$) as well as between $\delta^{18}O_{dw}$ and animal tooth enamel $\delta^{18}O_{phos}$ (*15*, *37*, *60*, *61*, *63–66*). These relationships can be formalized in regression equations and inverted to yield $\delta^{18}O_{dw}$ and air temperature from tooth enamel $\delta^{18}O$. Both the regression procedure and inversion can be accomplished using different statistical approaches (*37*, *64*). In this study we employ an inverted forward regression approach, where each regression line is established in the original causal direction and the resulting equation is then inverted to yield $\delta^{18}O_{dw}$ from tooth enamel $\delta^{18}O$ and temperature from drinking water/precipitation $\delta^{18}O$, following methods in ref.(*37*) (see below). Individual estimates for $\delta^{18}O_{dw}$ are pooled for each archaeological layer to yield an average temperature estimate for each layer with compound uncertainty. Compound uncertainties for layer temperature estimates are computed also following methods in ref.(*37*) and are used in order to quantify the propagated uncertainties incurred through both regression steps. All calculation steps for each conversion and uncertainty estimation can be found in the temperature conversion excel work sheets in the associated OSF online data repository. These excel sheets constitute filled out versions of the excel template published in ref. (*37*).

Enamel $\delta^{18}O_{phos}$ to $\delta^{18}O_{dw}$ regression lines used in this study were established using published data from bison (*65*) and cattle (*76*) for *Bos/Bison* values and data from horses published in refs.(*77*, *80*, *111*, *113*) for *Equus sp.*, which can be found in the associated data files and is plotted in Fig. S12. Using these data the relationship between $\delta^{18}O_{phos}$ to $\delta^{18}O_{dw}$ is obtained via least squares regression as

$$\delta^{18}O_{phos} = 0.85 \cdot \delta^{18}O_{dw} + 22.13$$

for *Bos/Bison*, and as

$$\delta^{18}O_{phos} = 0.87 \cdot \delta^{18}O_{dw} + 22.14$$

for Equids. Following ref.(*37*), these equations are then inverted to predict $\delta^{18}O_{dw}$ from $\delta^{18}O_{phos}$ as

$$\delta^{18}O_{dw} = \frac{\delta^{18}O_{phos} - 22.13}{0.85}$$

for *Bos/Bison*, and as

$$\delta^{18}O_{dw} = \frac{\delta^{18}O_{phos} - 22.14}{0.87}$$

for Equids.

A calibration data set for air temperature to $\delta^{18}O_{precip}$ was compiled using data from GNIP measurement stations (*18*) with a sufficient number of $\delta^{18}O_{precip}$ measurements (usually > 5 years for each monthly average) from Eastern, Southeastern, Central and Northern Europe and countries surrounding the Black Sea. In regions with sparse GNIP data, some stations with less than 5 years of measurements were included. The region from which GNIP data was sourced was deliberately chosen to be relatively large in order to cover a wide range of $\delta^{18}O_{precip}$ values and avoid calibrating archaeological values using extrapolated regions of the $\delta^{18}O_{precip}$ to temperature regression line (Fig. S10). This large geographic range of calibration data stations was also specifically chosen to account for the small spatial differences in the slope of the $\delta^{18}O_{precip}$-temperature regression, which is caused by differences in atmospheric circulation between locations (*58*, *81*, *91–94*). By including calibration data from a relatively large geographic area, such differences are included in the uncertainty around the palaeotemperature estimates, as they will impact the uncertainty of the regression coefficients. This approach is conceptually similar to the approach taken in ref.(*97*), who manually conducted several temperature conversions based on calibration data sets from different locations. It should be noted that unfortunately no data specifically from Bulgaria could be included, as Bulgaria does not have a GNIP station that measures $\delta^{18}O_{precip}$. As the slope of the temperature effect on $\delta^{18}O_{precip}$ is known to differ seasonally,(*93*, *94*, *114*) separate calibration data sets were used for summer, winter, and mean annual temperature conversions, which comprise data from 108, 107 and 78 stations respectively (see Fig. S11 for graphs of each temperature - $\delta^{18}O_{precip}$ regression). This also enables the temperature reconstructions to account for the differences in the amount of uncertainty in the temperature - $\delta^{18}O_{precip}$ regression between different seasons (Fig. S11). For summer and winter conversions, data from the warmest (commonly July or August) and coldest month (commonly

January or December) respectively were used. For mean annual temperature conversions, long-term mean annual averages as reported in the GNIP data base were used.

The least squares regression of the $\delta^{18}O_{precip}$-air temperature calibration data sets yields

$$\delta^{18}O_{precip} = 0.83 \cdot T - 11.52$$

for the coldest months,

$$\delta^{18}O_{precip} = 0.49 \cdot T - 13.76$$

for mean annual temperature and

$$\delta^{18}O_{precip} = 0.59 \cdot T - 14.2$$

for the warmest month. These equations are inverted analogously to the $\delta^{18}O_{phos}$ - $\delta^{18}O_{dw}$ relationships to estimate palaeotemperatures from precipitation oxygen isotopic compositions.

The two calibration steps are then combined to yield the complete conversion from tooth enamel $\delta^{18}O_{phos}$ to air temperature. The uncertainty of the final palaeotemperature estimate is therefore a compound uncertainty of the uncertainty of both conversion steps, where the uncertainty of the first regression needs to be propagated through the second regression step. Following error estimation in ref.(*37*), using a calibration data set containing a random sample of n values (x_i, yi) the uncertainty of the $\delta^{18}O_{dw}$ estimate for a $\delta^{18}O_{phos}$ input value of $x = x_0$ (δx_0) is estimated as

$$\delta x_0 = \frac{s_{y/x}}{a} \cdot \sqrt{\frac{1}{m} + \frac{1}{n} + \frac{(y_0 - \overline{y})^2}{a^2 \sum (x_i - \overline{x})^2}}$$

, where $s_{y/x}$ is an estimate of the standard deviation of the natural sample variability, a is the slope parameter and $\overline{x}$ and $\overline{y}$ are the means of the calibration data set.

This uncertainty around the $\delta^{18}O_{dw}$ estimate is then used to further infer the uncertainty of the palaeotemperature estimate at temperature $T = T_0$ (δT_0), which is estimated analogously as

$$\delta T_0 = \frac{1}{a_T} \cdot \sqrt{\delta x_0^2 + \frac{s_{x/T}^2}{n_T} + \frac{s_{x/T}^2 (x_0 - \overline{x}_T)^2}{a_T^2 \sum (T_i - \overline{T})^2}}$$

, where δx_0 replaces the sample variability $\frac{s_{x/T}}{\sqrt{m}}$. As can the seen from the equations above, the palaeotemperature uncertainty estimate accounts for: 1) the uncertainty in the regression line caused by the natural variability of the samples in the calibration data sets, 2) the variability of

the samples used for palaeotemperature reconstruction around their population mean, 3) the propagation of these errors through both regression steps. In this way, the uncertainty of the palaeotemperature estimate decreases with a larger calibration data set, a larger sample data set, and when palaeotemperature estimation is undertaken closer to the mean of the calibration data set (i.e. with the least amount of extrapolation). A detailed description of how these equations are derived can be found in ref.(*37*) and error estimation calculations for our data set can be found in the temperature estimation excel files provided in the associated OSF repository.

It should be noted that the error estimation used here does not take into account the measurement error of either samples or calibration data, or the uncertainty associated with converting between $\delta^{18}O$ from the phosphate and the carbonate fraction, as these sources of error are very small compared to the uncertainty incurred through the calibration regression steps (*37*). In this study, all samples and the vast majority of calibration data were measured as $\delta^{18}O_{phos}$ on the phosphate fraction, with only a small portion of the calibration data having to be converted from $\delta^{18}O$ of the carbonate fraction (N = 13 out of N_{total} = 62). The references providing the equations for converting between $\delta^{18}O_{phos}$ and $\delta^{18}O_{carb}$ and between the VPDB and VSMOW scales (used for 2 calibration data points), are noted in the data file of the $\delta^{18}O_{phos}$ to $\delta^{18}O_{dw}$ calibration data.

To generate summer and winter palaeotemperature estimates, summer peaks and winter troughs from the inverse model described in Supplementary Text S7 were used as input values for the temperature conversion. In contrast, mean annual temperatures were generated directly from unmodelled values $\delta^{18}O_{phos}$ values. This process was chosen as the inverse model stretches $\delta^{18}O$ time series curves in a relatively symmetrical manner and therefore has very little impact on averaged $\delta^{18}O$ values (two-point mean of modelled $\delta^{18}O$), but introduces substantial uncertainty compared to the raw $\delta^{18}O_{phos}$ values. Mean annual values were calculated as the mean of the summer peak and the winter trough value (two-point mean of unmodelled $\delta^{18}O$), analogous to calculations of modern-day mean annual temperatures. Mean annual $\delta^{18}O$ values could theoretically also be obtained by calculating an average of all unmodelled $\delta^{18}O$ values over the span of one year (i.e. winter trough to winter trough) to obtain an annual mean of unmodelled $\delta^{18}O$. A comparison of these different methods for obtaining mean annual $\delta^{18}O$ values (two-point mean of unmodelled $\delta^{18}O$, annual mean of unmodelled $\delta^{18}O$, two-point mean of modelled $\delta^{18}O$) shows, that different averaging methods have very little impact on the obtained mean $\delta^{18}O$ values (Fig. S6) or on the final mean annual temperature estimates (Fig. S7). We therefore chose the option of the two-point unmodelled average, which allows for the highest number of data

points (as some $\delta^{18}O$ series have several peaks and troughs, but not several complete years), has comparatively low uncertainty, and is most comparable to modern air temperature data. Summer peaks and winter troughs of $\delta^{18}O$ curves were isolated by visual inspection as maximum and minimum values of each sinusoidal curve (see Supplementary Text S6).

Due to species-specific isotopic offsets between tooth enamel $\delta^{18}O$ and drinking water $\delta^{18}O$ values ($\delta^{18}O_{dw}$), oxygen isotope delta values of tooth enamel need to be converted to equivalent $\delta^{18}O$ drinking water values to compare different species. We use this here to establish that *Bos/Bison* and *Equus sp.* yield comparable $\delta^{18}O$ results at Bacho Kiro Cave and can be combined for temperature estimation.

A comparison between *Bos/Bison* and *Equus sp.* $\delta^{18}O_{dw}$ values for Bacho Kiro Layer N1-I & I can be seen in Fig. S8. *Bos/Bison* $\delta^{18}O_{dw}$ values fall within the range of variation within error of *Equus sp.* $\delta^{18}O_{dw}$ values, although they commonly fall on the upper end of the *Equus sp.* range. Considering the uncertainty introduced by the drinking water value conversion, the two taxa are in good agreement. $\delta^{18}O_{dw}$ of both taxa are therefore combined to yield a more precise and robust temperature estimate for Layer N1-I & I. Resulting temperature estimates can be found in the results section of the main manuscript.

S9. Strontium isotope analysis

Subsample aliquots of each sequential tooth enamel sample were reserved as enamel pieces for strontium isotope analysis prior to grinding of samples for oxygen isotope analysis. Two samples, representing the summer and winter season input, were chosen for a subset of individuals to be analysed for $^{87}Sr/^{86}Sr$. To be able to compare summer and winter $^{87}Sr/^{86}Sr$ to capture any potential seasonal migrations, only individuals with both summer peaks and winter troughs were analysed for $^{87}Sr/^{86}Sr$.

Enamel pieces were first transferred to a PicoTrace clean laboratory facility at the MPI-EVA, and cleaned in the facility prior to sample preparation. Enamel pieces were cleaned by sonication in Milli-Q ultrapure water for 10 minutes, rinsed first with Milli-Q ultrapure water and then acetone and then left to dry prior to sample preparation.

Sample digestion and ion-exchange chromatography was conducted following methods described in ref.(*35*). Briefly, ca. 10 mg of tooth enamel were weighed into cleaned 7 mL Teflon beakers (Savillex, Eden Prairie, USA) and digested in 2 mL of 65% HNO_3 (Merck SupraPur grade, Merck, Darmstadt, Germany) for 2 hours at 120 °C and the solution then evaporated to dryness. The

resulting residue was re-dissolved in 1 mL of 3N HNO_3 at 120 °C for 1 hour. The sample solution was then loaded onto a 0.5 cm bed of cleaned and pre-conditioned 50-100 μm Sr-spec resin (EiChrom Technologies, Lisle, USA) placed in cleaned microcolumns. All sample solutions were passed through the column step 4 times to ensure complete loading of strontium onto the ion-exchange resin. Matrix elution was achieved using 3 times 400 μL of 3N HNO_3, after which strontium was eluted from the columns using 1.5 mL of MilliQ ultrapure water. The resulting Sr containing solution was evaporated to dryness at 120 °C and re-dissolved in 1 mL of 3 % HNO_3. Two process blanks were prepared alongside samples to assess the level of contamination during the sample preparation procedure. Additionally, two aliquots of the NIST SRM 1486 bone meal standard were treated with the samples to serve as a quality control standard. All samples were analysed for $^{87}Sr/^{86}Sr$ using a Neptune Multi-Collector Inductively Coupled Plasma Mass Spectrometer (MC-ICPMS, Thermo Fisher Scientific, Bremen, Germany) at the MPI-EVA. $^{87}Sr/^{86}Sr$ measurements were normalised for instrumental mass bias to $^{88}Sr/^{86}Sr = 8.375209$ (exponential law) and corrected for ^{87}Rb interference. External data normalisation was conducted using the NIST SRM 987 reference material ($^{87}Sr/^{86}Sr$ accepted value = 0.710240 (*36*); average of measured values = 0.710283 $\pm$ 0.000009 (1 s.d., n = 16)) using correction offsets of -0.000042 and -0.000043. Measurements of NIST SRM 1486 gave an average value of 0.709296 $\pm$ 0.0000056 (1 s.d., 4 measurements of 2 aliquots), which is very close to the expected value of 0.709299. All samples were measured in duplicate with an average reproducibility of 0.0000068 (1 s.d.). Procedural blanks gave Sr concentrations of ca. 0.02 % of typical sample concentrations. A lack of relationship between sample strontium concentration and $^{87}Sr/^{86}Sr$ values indicates that samples did not take up substantial amounts of Sr from the depositional environment and therefore preserve a biogenic strontium isotope ratio (Fig. S9). All strontium isotope measurements can be found in Table S3. Strontium isotope analysis of enamel samples formed in summer and winter do not show substantial differences in $^{87}Sr/^{86}Sr$ between the seasons for any of the analysed individuals (Fig. S5). As $^{87}Sr/^{86}Sr$ values of tooth enamel reflect $^{87}Sr/^{86}Sr$ values of underlying lithological units, this indicates that animals did not undertake seasonal movements across different lithological units. These results are therefore consistent with non-migratory animals that record a faithful signal of climate driven oxygen isotope ratios in local environmental water, without bias from geo-spatial variation of $\delta^{18}O$ of precipitation. Our oxygen isotope results can therefore be used for local climatic reconstructions.

Due to the lack of comparative $^{87}Sr/^{86}Sr$ data for the lithological units in the area around Bacho Kiro Cave, we cannot definitively determine the origin of the animals sampled here. However, $^{87}Sr/^{86}Sr$ values of tooth enamel samples fall close to the upper end of $^{87}Sr/^{86}Sr$ values observed

globally in sedimentary carbonate lithologies (*115*). $^{87}Sr/^{86}Sr$ of our samples therefore could be consistent with animals ranging across a mixture of karst bedrock and other lithological units with higher $^{87}Sr/^{86}Sr$ values. Due to the lack of migratory signature in the seasonal $^{87}Sr/^{86}Sr$ values of tooth enamel, these are most likely other lithologies in the vicinity of Bacho Kiro Cave, such as sandstone and non-carbonate sedimentary lithologies.

S10. Software and code

This article, including code for all data analyses, was written in R (version 3.6.2) (*39*) on a Windows 10 operating system and the manuscript rendered using RMarkdown (*40*). The code for data analysis and manuscript and SI rendering makes use of the rstatix_0.6.0 (*116*), tidyr_1.0.2 (*117*), captioner_2.2.3 (*118*), flextable_0.5.11 (*119*), ggplot2_3.3.2 (*120*), stringr_1.4.0 (*121*), dplyr_1.0.2 (*122*), knitr_1.29 (*123*), officer_0.3.14 (*124*), ggmap_3.0.0 (*125*), pander_0.6.3 (*126*), gridExtra_2.3 (*127*), magick_2.4.0 (*128*), patchwork_1.0.1 (*129*), ggpubr_0.4.0 (*130*), cowplot_1.1.0 (*131*), and redoc(*132*) packages. Data and code to reproduce the manuscript files, figures and analyses are available at https://osf.io/tk9dc/.

11. Supplementary Figures

Fig. S1: Map of the location of Bacho Kiro Cave in north central Bulgaria. Basemap obtained from OpenStreetMap (*133*).

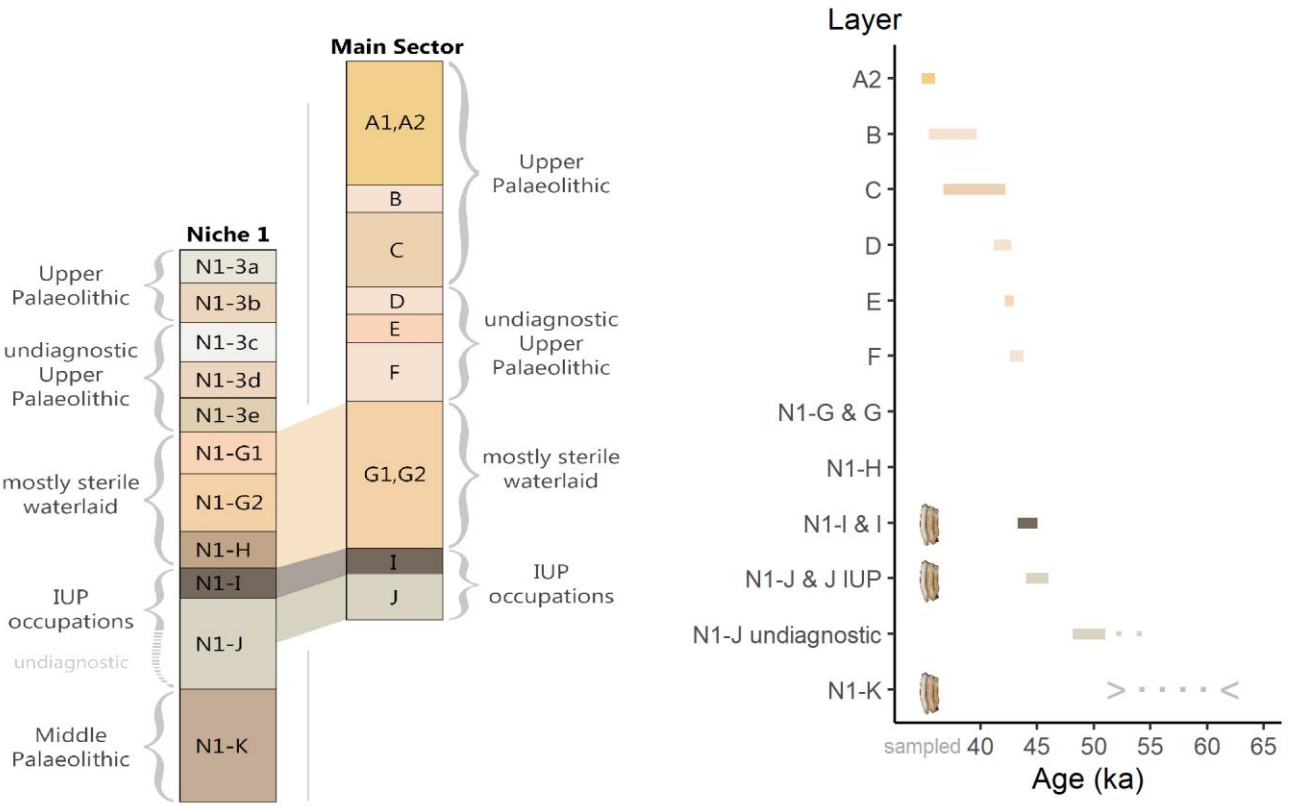

Fig. S2: Bacho Kiro Cave stratigraphy and chronology. The 2015-2019 excavations in the Main Sector and the Niche 1 sector at Bacho Kiro Cave uncovered a stratigraphic sequence with Middle Paleolithic, Initial Upper Palaeolithic and Upper Palaeolithic deposits. Radiocarbon and OSL dates show that these deposits cover ages from the beginning of MIS 3 at around 61 ka to ~ 34 ka. The IUP layers as well as overlying waterlaid deposits can be well correlated between the Main Sector and the Niche 1, as visualised by shaded connections. Layers where faunal samples were taken for isotope analyis are marked with small tooth icons.

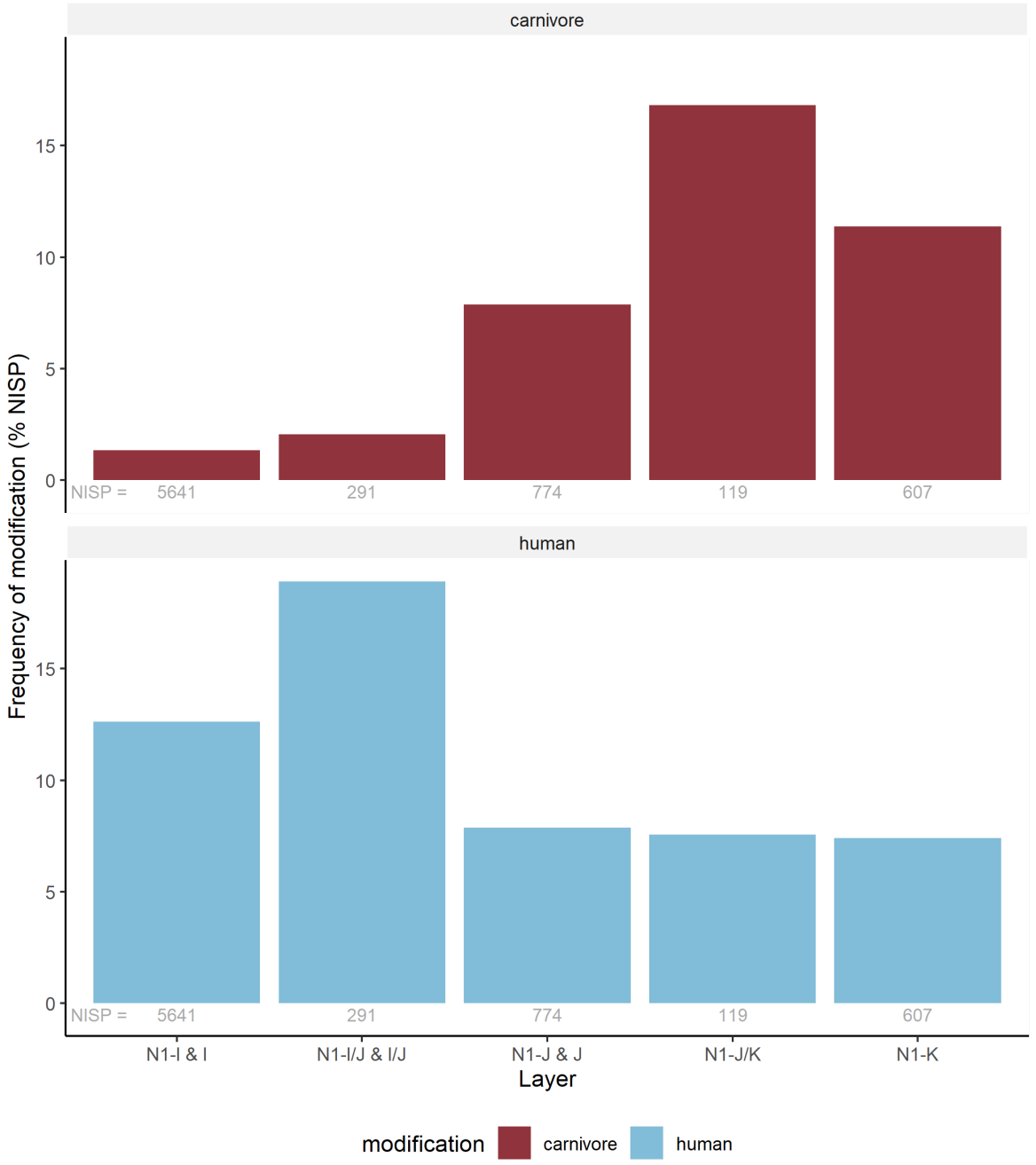

Fig. S3: Bone surface modifications of faunal remains. Relative frequencies of human (blue) and carnivore (red) surface modifications on ungulate bones relative to total NISP (printed below bars) grouped by layer underline the anthropogenic nature of the IUP faunal assemblage (Layer N1-I & I and contact to N1-J & J). Carnivore modifications become more frequent in the Middle Palaeolithic layer (N1-K) and in the lower parts of the IUP sequence (N1-J).

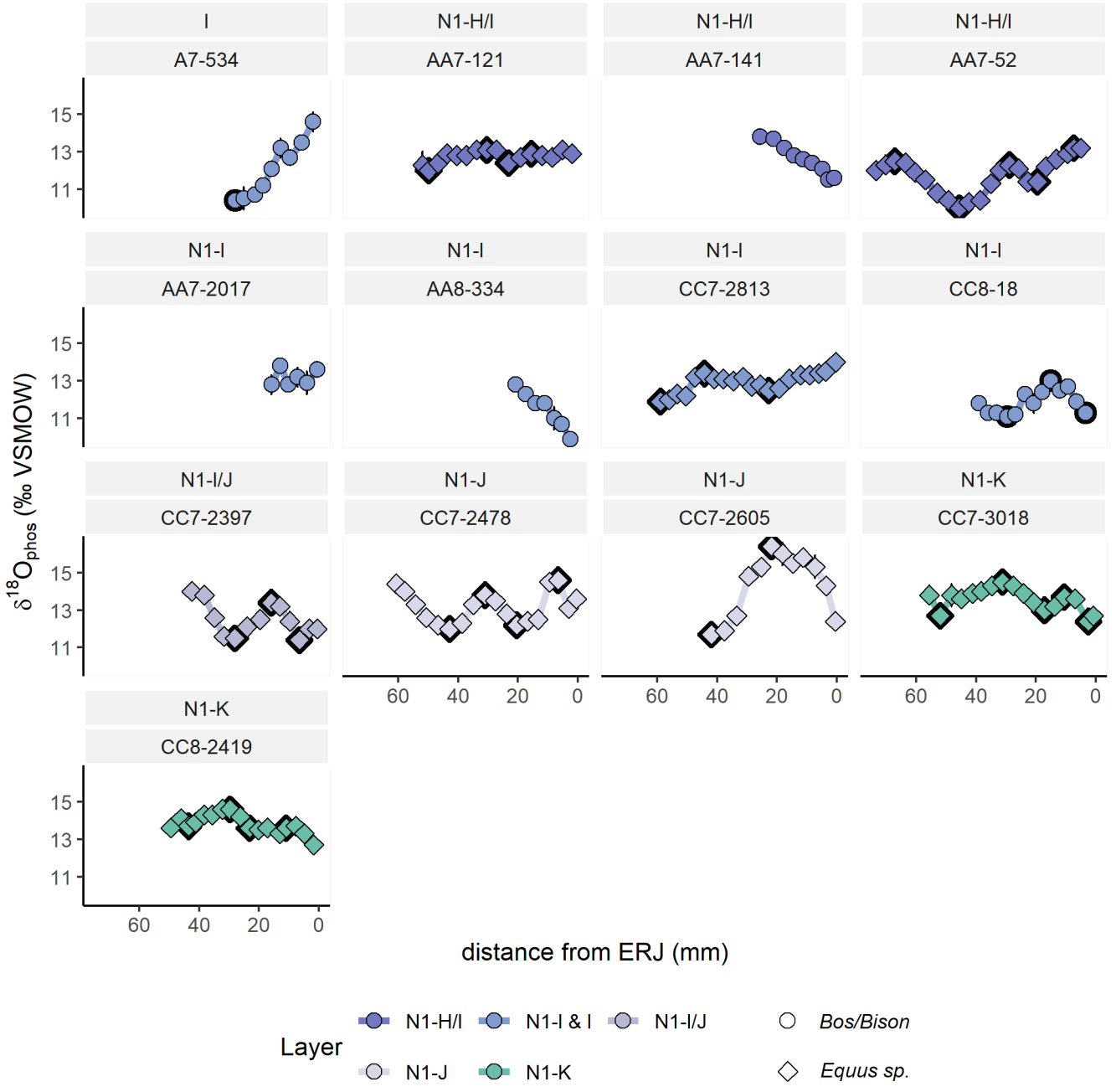

Fig. S4: Oxygen isotope seasonal curves from measurement series of sequential tooth enamel samples. Sequentially sampled tooth enamel of *Equus sp.* (diamonds) and *Bos/Bison* (circles) individuals show full or partial sinusoidal curves of seasonal change in $\delta^{18}O_{phos}$. Error bars (often smaller than point symbols) represent one standard deviation around the mean of replicate measurements. Individuals are ordered and coloured by layer from top to bottom (also noted in top panel titles). Individual find numbers are noted in lower panel titles. Summer peak and winter trough values that were used to examine seasonal climatic conditions are marked in bold.

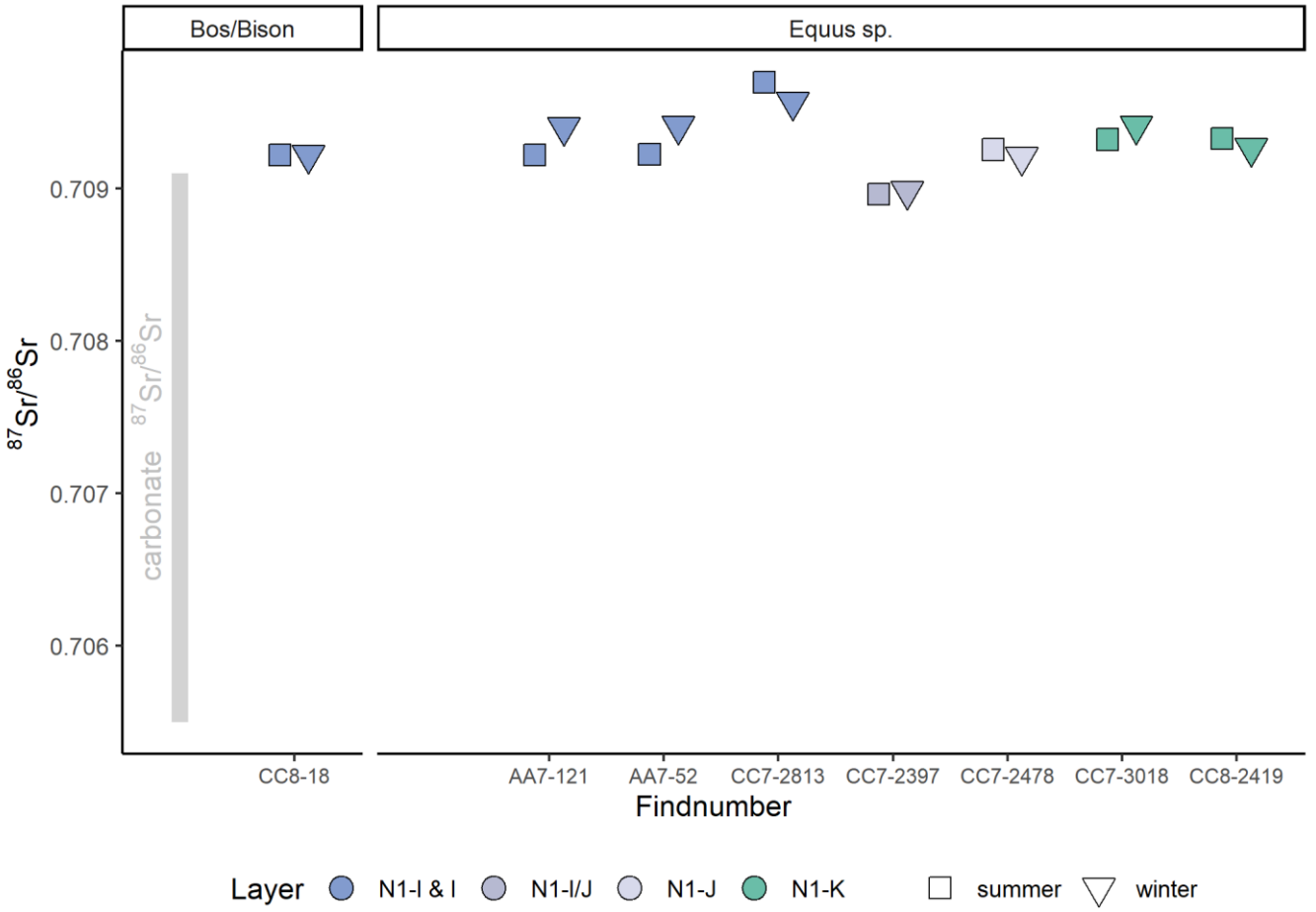

Fig. S5: Summer and winter strontium isotope data. $^{87}Sr/^{86}Sr$ values of horses (right) and aurochs/bison (left) do not show substantial or systematic differences between summer (squares) and winter (triangles), indicating a lack of seasonal long distance movement by these animals. Values fall in the upper range and slightly above the range of $^{87}Sr/^{86}Sr$ typical for carbonate lithologies(*115*) (grey bar), possibly due to input of Sr from nearby sandstone and non-carbonate sedimentary lithologies present in the vicinity of Bacho Kiro Cave.

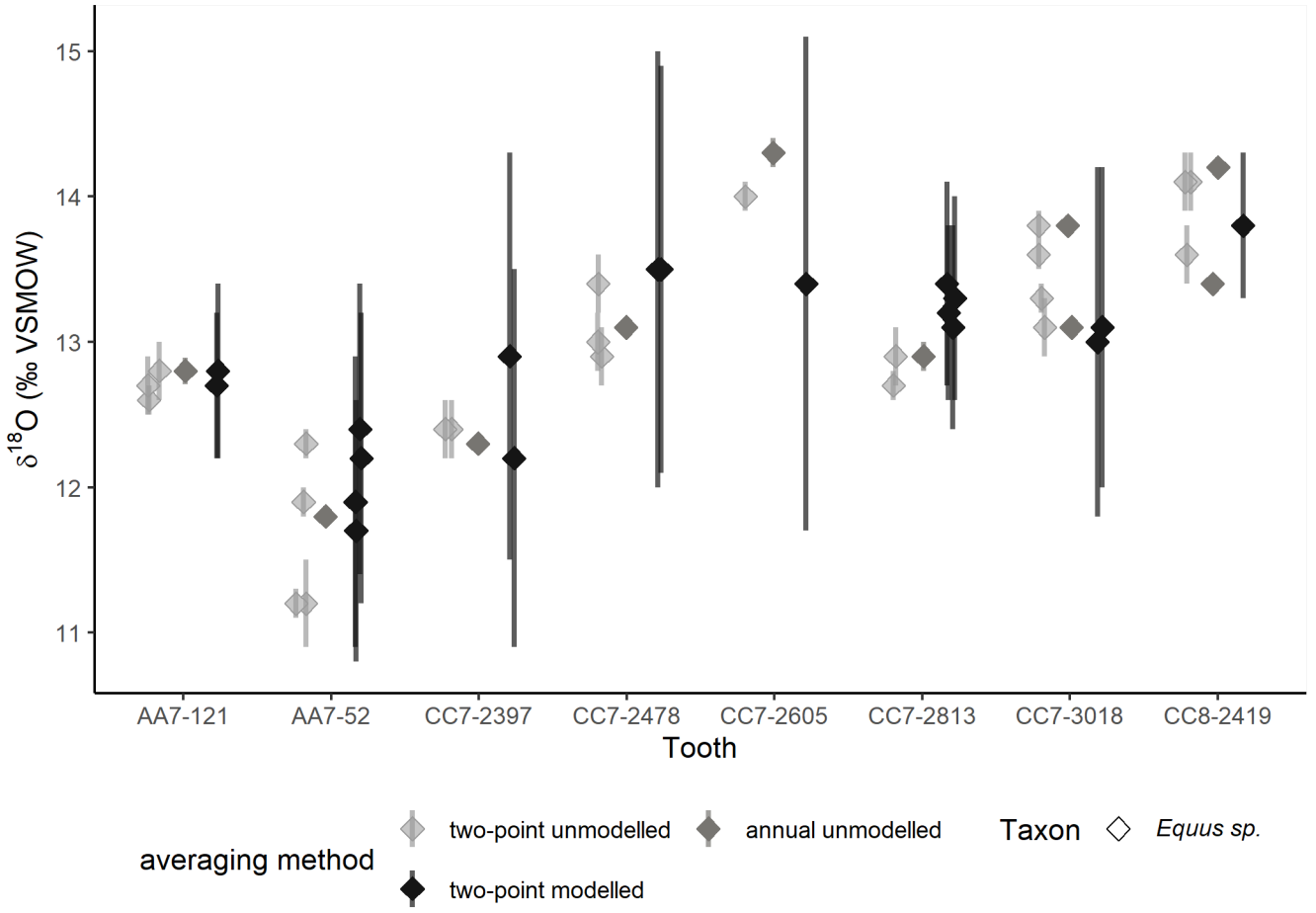

Fig. S6: Comparison of different averaging methods for obtaining mean annual oxygen isotope delta values. Mean annual values calculated as the two-point mean of unmodelled δ^{18}O (light grey, left); annual mean of unmodelled δ^{18}O (medium grey, middle), or two-point mean of modelled δ^{18}O (dark grey, right), yield comparable results for all analysed teeth. Error bars represent the error of the mean propagated from measurement uncertainty in the case of unmodelled values or propagated from the 1 s.d. uncertainty of the inverse model for modelled values. Different methods are compared here using the example of *Equus sp.* data.

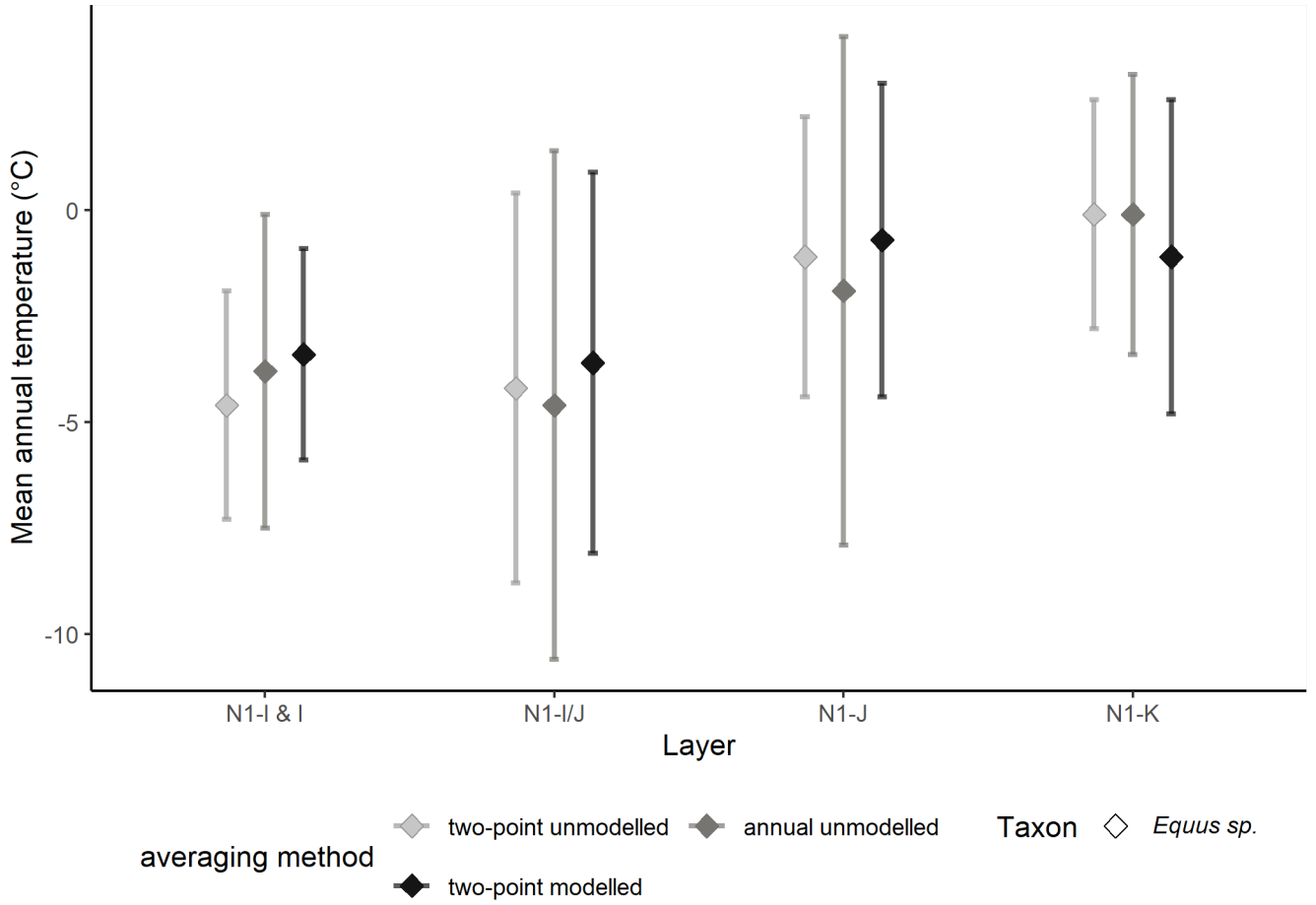

Fig. S7: Comparison of mean annual temperatures reconstructed from mean annual oxygen isotope delta values obtained via different averaging methods. Mean annual temperratures from mean annual oxygen isotope values calculated via different methods (two-point mean of unmodelled δ^{18}O - light grey, left; annual mean of unmodelled δ^{18}O - medium grey, middle; and two-point mean of modelled δ^{18}O - dark grey, right) are extremely similar to each other for all considered archaeological layers. Error bars represent the compound error around the temperature estimate. Different methods are compared here using the example of *Equus sp.* data.

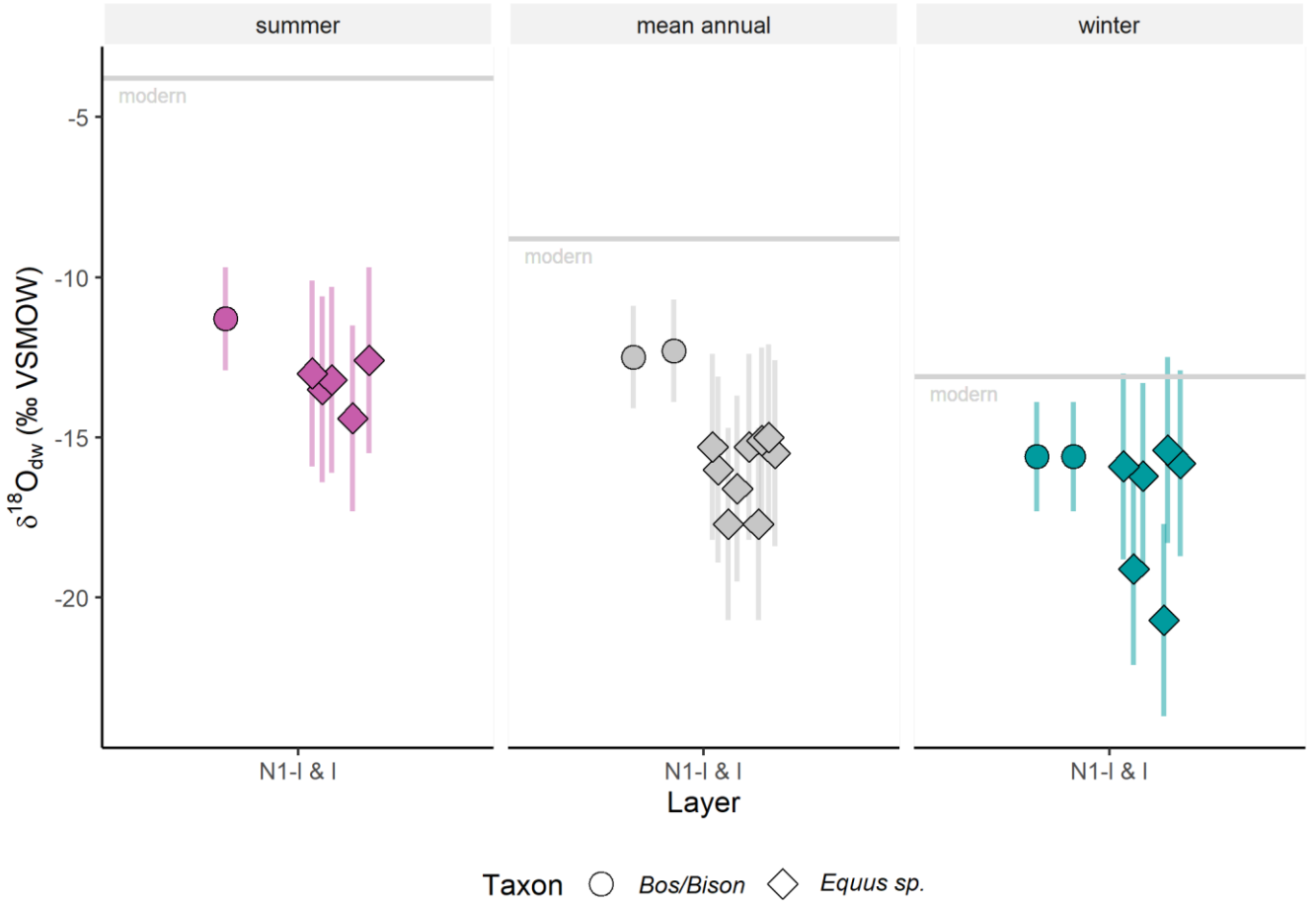

Fig. S8: Reconstructed oxygen isotope composition of drinking water. *Equus sp.* (diamonds) and *Bos/Bison* (circles) show good agreement in reconstructed oxygen isotope values of drinking water ($\delta^{18}O_{dw}$), with *Bos/Bison* values at the upper end but overlapping with *Equus sp.* variability in summer (pink, left), mean annual (grey, middle) and winter (blue, right) values. Agreement between the different species indicates robustness of $\delta^{18}O$ values as a climate proxy and enables combining the two taxa for further temperature reconstruction. Estimates of modern-day precipitation $\delta^{18}O$ (grey lines) are interpolated estimates obtained from the Online Isotopes in Precipitation Calculator (OIPC)(*16–18*).

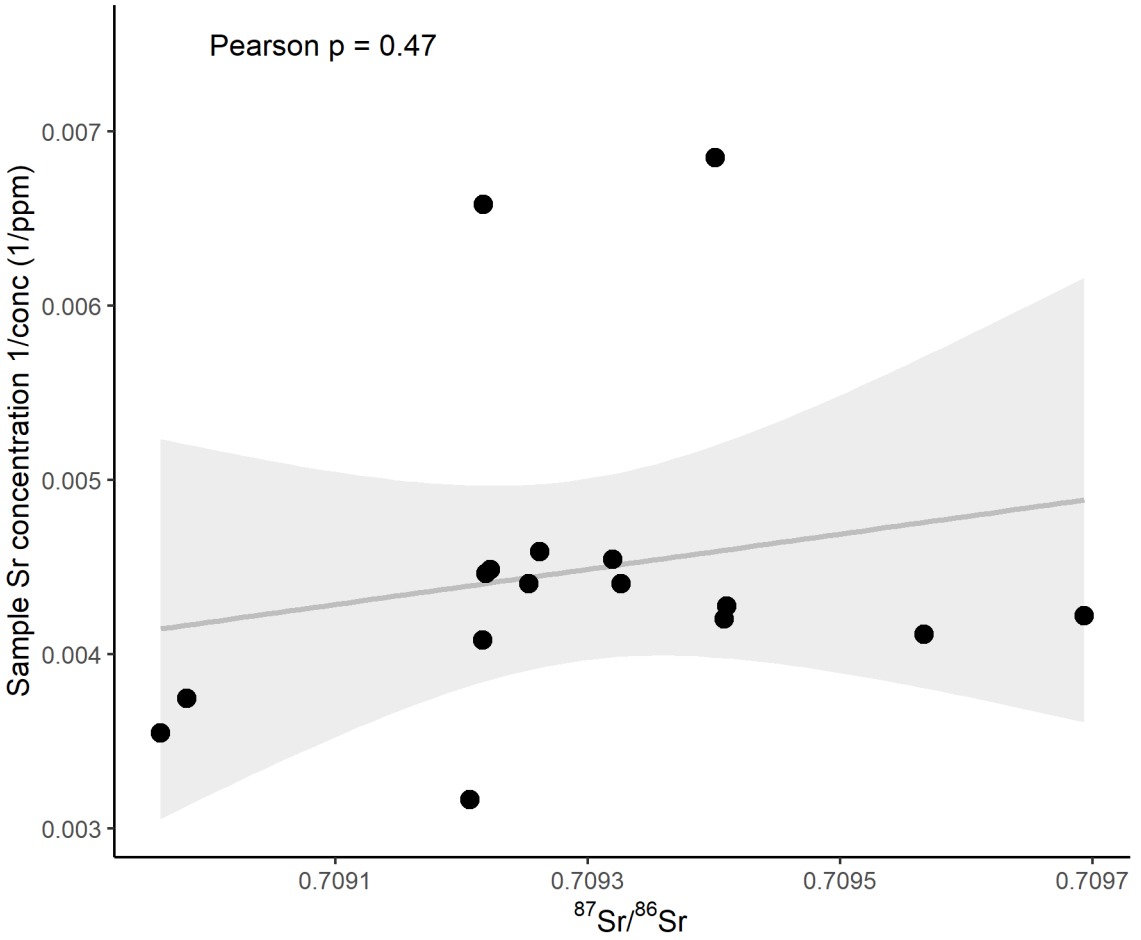

Fig. S9: Relationship between Sr concentration and Sr isotope value. Absence of a relationship between Sr isotope values and Sr concentration (Pearson correlation p = 0.3) in archaeological samples indicates a lack of significant post depositional Sr uptake.

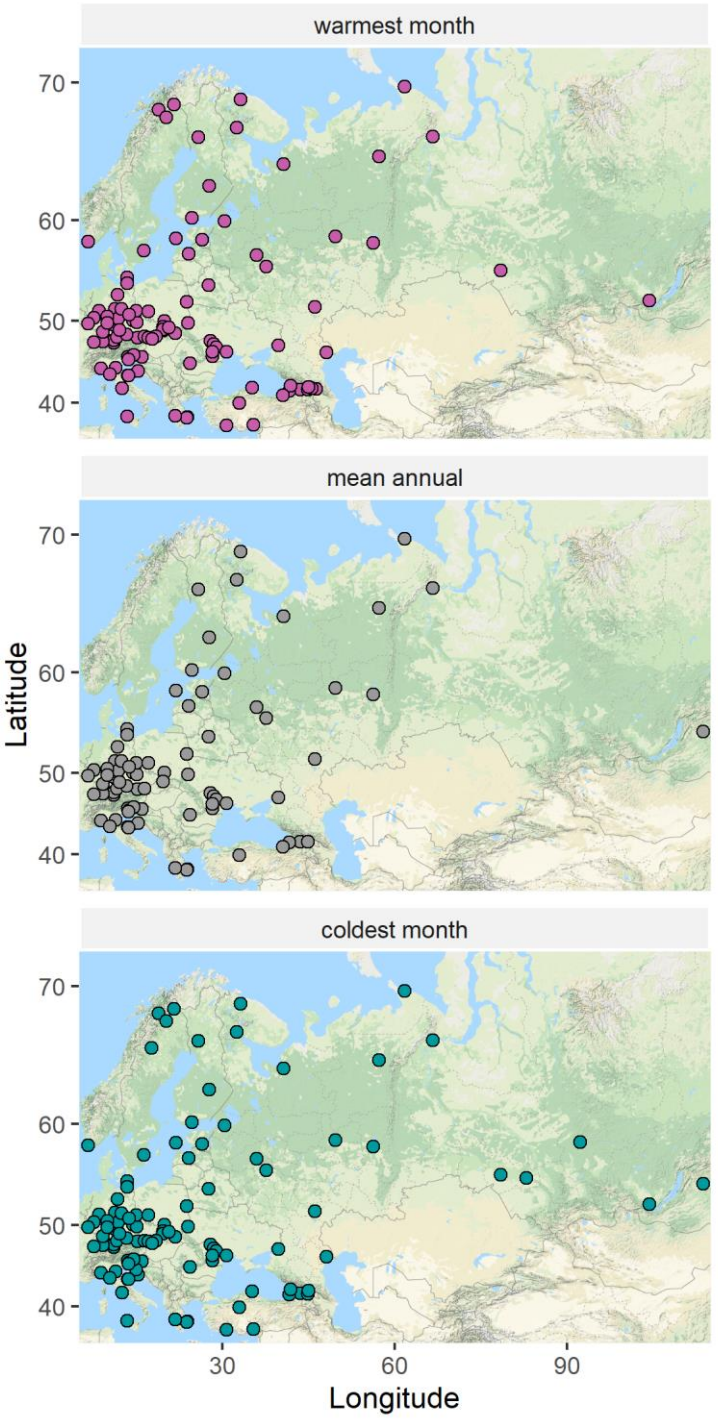

Fig. S10: Location of GNIP stations used for oxygen isotope to temperature conversion calibration data. Location of GNIP stations that were used to obtain water isotope and air temperature data for the warmest month (top), mean annual (middle) and coldest month (bottom). GNIP stations were chosen to cover a large range of temperatures and circulation regimes.

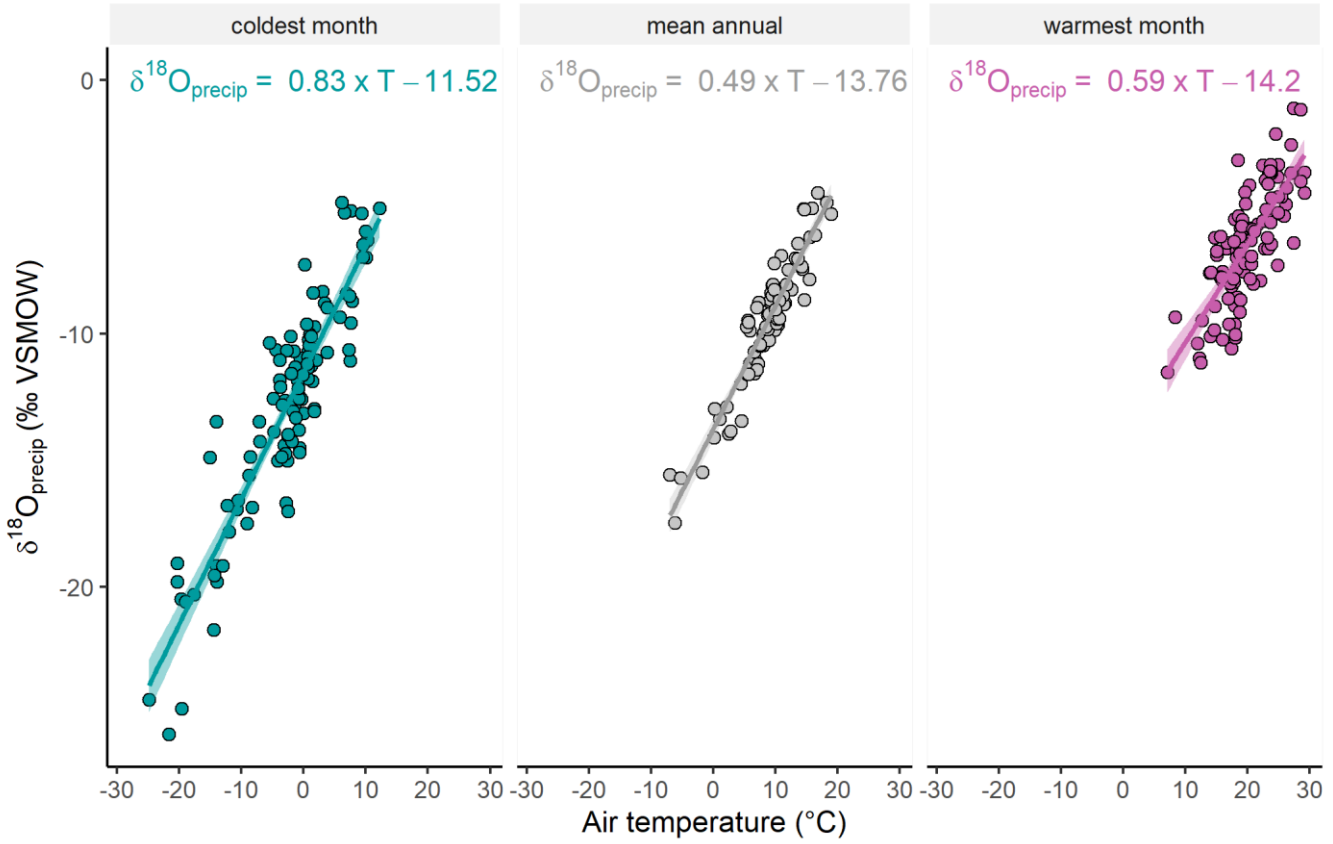

Fig. S11: Calibration data sets of GNIP station air temperature and $\delta^{18}O_{precip}$ data. These data were used to establish the regression relationship between temperature and water oxygen isotope values for the warmest month, mean annual and coldest month. Regression lines and shaded areas represent an OSL linear model with a 95% confidence interval, and are shown to illustrate the differences in regression uncertainty between the data sets, but do not represent the actual uncertainty incorporated in the compound error calculation of temperature estimates. Regression equations used in the temperature calibration are displayed on the graphs and uncertainty calculations can be found in the temperature conversion excel files provided in the associated data repository.

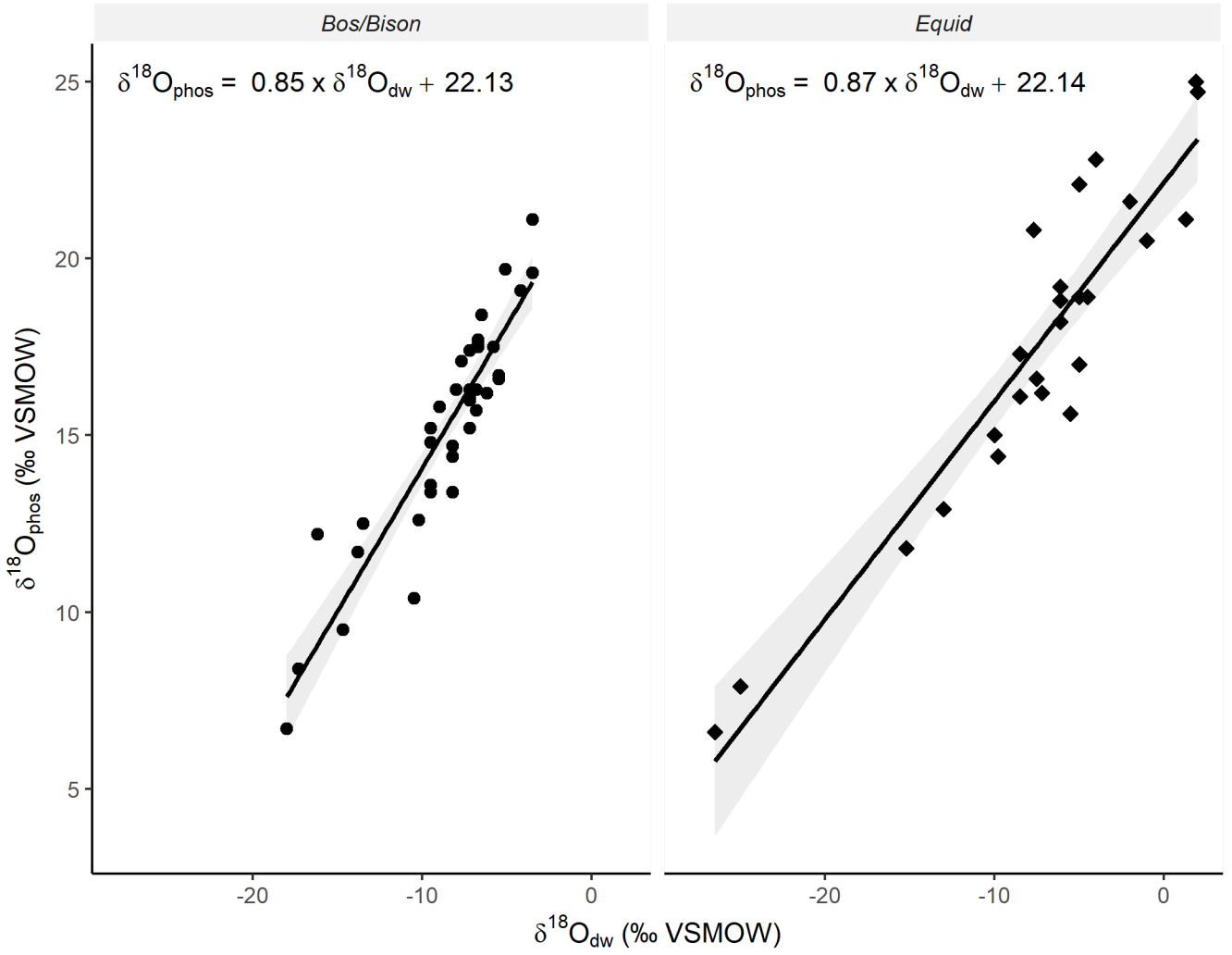

Fig. S12: Calibration data sets of tooth enamel and drinking water and $\delta^{18}O$ data. These data were used to establish the regression relationship between tooth enamel and drinking water oxygen isotope values for *Bos/Bison* and Equids and was obtained from refs. (*65*, *76*, *77*, *80*, *111*, *113*). The resulting regression line, following methods in ref.(*37*), is printed on the plot. Regression lines and shaded areas represent an OSL linear model with a 95% confidence interval, and are shown to illustrate the differences in regression uncertainty in different areas of the curve, but do not represent the actual uncertainty incorporated in the compound error calculation of temperature estimates. Regression equations used in the drinking water calibration are displayed on the graphs and uncertainty calculations can be found in the temperature conversion excel files provided in the associated data repository.

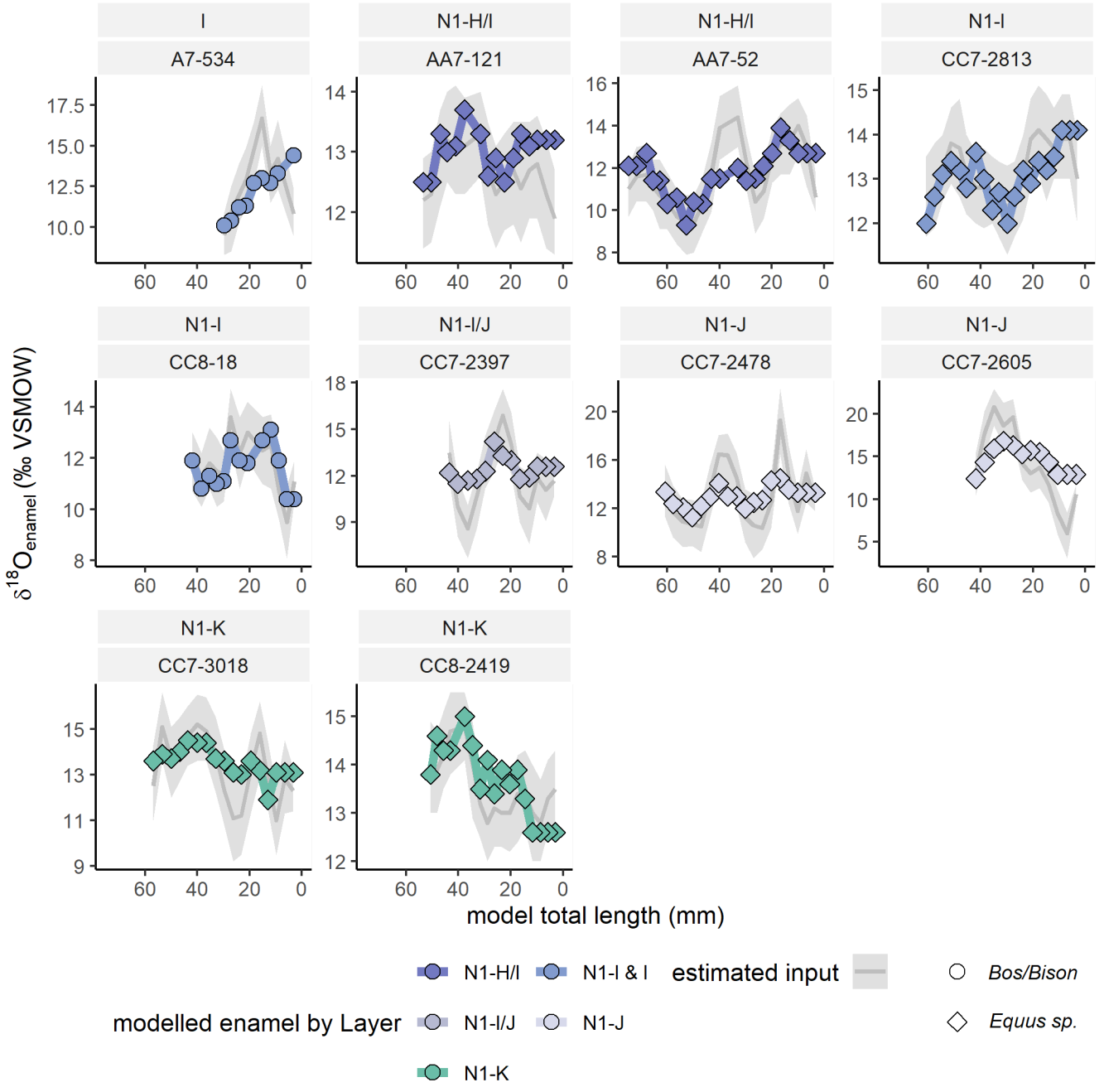

Fig. S13: Oxygen isotope input inverse model results. Mean estimated $\delta^{18}O$ input (grey line) with 95% confidence interval (grey shaded area) and dMeasd variable modelled tooth enamel $\delta^{18}O$ values from Passey et al. (*38*) inverse models for *Bos/Bison* (circles) and *Equus sp.* (diamonds) individual teeth (find numbers are noted in top panel titles). dMeasd time series are coloured by layer (also noted in top panel titles). Note that y-axis limits differ between plots to accommodate visualisation of seasonal $\delta^{18}O$ change.

12. Supplementary Tables

Table S1: Dosimetry data and equivalent dose (De) obtained from sample L-EVA 1786. (continued below)

Field code	Sample ID	U (ppm)	error (ppm)	Th (pmm)	error (ppm)	K (%)	error (%)	H_2O (%)
Bk-k, CC7-2800	L-EVA 1786	3.5	0.3	4.6	0.3	0.68	0.1	16

error (%)	Total doserate (mGy/a)	error (mGy/a)	De $pIRIR_{290}$ (Gy)	error (Gy)	$pIRIR_{290}$ age (ka)	error (ka)
10	2.21	0.2	134	3	60.6	5.9

Table S2: Oxygen isotope values and standard deviations of replicate measurements for all sequential tooth enamel samples presented in this study. Sup. - maxillary, inf. - mandibular.

Sample ID	Tooth	Layer	Taxon	Tooth position	mm from ERJ	$\delta^{18}O$	SD
A7-534.A	A7-534	I	*Bos/Bison*	M2 inf.	28.0	10.4	0.2
A7-534.D	A7-534	I	*Bos/Bison*	M2 inf.	25.1	10.5	0.6
A7-534.G	A7-534	I	*Bos/Bison*	M2 inf.	21.4	10.7	0.2
A7-534.J	A7-534	I	*Bos/Bison*	M2 inf.	18.6	11.2	0.2
A7-534.M	A7-534	I	*Bos/Bison*	M2 inf.	15.7	12.1	0.4
A7-534.P	A7-534	I	*Bos/Bison*	M2 inf.	12.8	13.2	0.5
A7-534.S	A7-534	I	*Bos/Bison*	M2 inf.	9.6	12.7	0.4
A7-534.V	A7-534	I	*Bos/Bison*	M2 inf.	5.7	13.5	0.3
A7-534.Y	A7-534	I	*Bos/Bison*	M2 inf.	1.9	14.6	0.5
AA7-121.B	AA7-121	N1-H/I	*Equus sp.*	M2 sup.	51.9	12.3	0.7
AA7-121.D	AA7-121	N1-H/I	*Equus sp.*	M2 sup.	49.9	12.0	0.2
AA7-121.G	AA7-121	N1-H/I	*Equus sp.*	M2 sup.	46.7	12.4	0.1
AA7-121.J	AA7-121	N1-H/I	*Equus sp.*	M2 sup.	43.8	12.9	0.3
AA7-121.M	AA7-121	N1-H/I	*Equus sp.*	M2 sup.	40.5	12.8	0.4
AA7-121.P	AA7-121	N1-H/I	*Equus sp.*	M2 sup.	37.3	12.8	0.1
AA7-121.S	AA7-121	N1-H/I	*Equus sp.*	M2 sup.	33.8	13.1	0.3
AA7-121.V	AA7-121	N1-H/I	*Equus sp.*	M2 sup.	30.4	13.1	0.2
AA7-121.Y	AA7-121	N1-H/I	*Equus sp.*	M2 sup.	27.3	13.1	0.3
AA7-121.AB	AA7-121	N1-H/I	*Equus sp.*	M2 sup.	23.2	12.4	0.4
AA7-121.AE	AA7-121	N1-H/I	*Equus sp.*	M2 sup.	19.2	12.7	0.1
AA7-121.AH	AA7-121	N1-H/I	*Equus sp.*	M2 sup.	15.6	12.9	0.2
AA7-121.AK	AA7-121	N1-H/I	*Equus sp.*	M2 sup.	12.0	12.8	0.2
AA7-121.AN	AA7-121	N1-H/I	*Equus sp.*	M2 sup.	8.6	12.7	0.5

Sample ID	Tooth	Layer	Taxon	Tooth position	mm from ERJ	$\delta^{18}O$	SD
AA7-121.AQ	AA7-121	N1-H/I	*Equus sp.*	M2 sup.	5.2	13.1	0.4
AA7-121.AT	AA7-121	N1-H/I	*Equus sp.*	M2 sup.	2.0	12.9	0.2
AA7-141.A	AA7-141	N1-H/I	*Bos/Bison*	M3 inf.	25.7	13.8	0.4
AA7-141.D	AA7-141	N1-H/I	*Bos/Bison*	M3 inf.	21.1	13.7	0.2
AA7-141.G	AA7-141	N1-H/I	*Bos/Bison*	M3 inf.	17.5	13.2	0.1
AA7-141.J	AA7-141	N1-H/I	*Bos/Bison*	M3 inf.	14.3	12.8	0.2
AA7-141.M	AA7-141	N1-H/I	*Bos/Bison*	M3 inf.	11.3	12.6	0.2
AA7-141.P	AA7-141	N1-H/I	*Bos/Bison*	M3 inf.	8.2	12.4	0.2
AA7-141.S	AA7-141	N1-H/I	*Bos/Bison*	M3 inf.	4.9	12.1	0.3
AA7-141.U	AA7-141	N1-H/I	*Bos/Bison*	M3 inf.	2.8	11.5	0.2
AA7-141.W	AA7-141	N1-H/I	*Bos/Bison*	M3 inf.	0.8	11.6	0.3
AA7-2017.A	AA7-2017	N1-I	*Bos/Bison*	M3 inf.	15.8	12.8	0.5
AA7-2017.D	AA7-2017	N1-I	*Bos/Bison*	M3 inf.	12.9	13.8	0.2
AA7-2017.G	AA7-2017	N1-I	*Bos/Bison*	M3 inf.	10.2	12.8	0.3
AA7-2017.J	AA7-2017	N1-I	*Bos/Bison*	M3 inf.	7.1	13.2	0.5
AA7-2017.M	AA7-2017	N1-I	*Bos/Bison*	M3 inf.	4.0	12.9	0.6
AA7-2017.P	AA7-2017	N1-I	*Bos/Bison*	M3 inf.	0.6	13.6	0.4
AA7-52.A	AA7-52	N1-H/I	*Equus sp.*	M3 inf.	73.5	12.0	0.3
AA7-52.D	AA7-52	N1-H/I	*Equus sp.*	M3 inf.	70.3	12.3	0.5
AA7-52.G	AA7-52	N1-H/I	*Equus sp.*	M3 inf.	67.2	12.5	0.6
AA7-52.J	AA7-52	N1-H/I	*Equus sp.*	M3 inf.	63.7	12.4	0.2
AA7-52.M	AA7-52	N1-H/I	*Equus sp.*	M3 inf.	60.4	11.9	0.4
AA7-52.P	AA7-52	N1-H/I	*Equus sp.*	M3 inf.	57.0	11.5	0.3
AA7-52.S	AA7-52	N1-H/I	*Equus sp.*	M3 inf.	53.1	10.8	0.4
AA7-52.V	AA7-52	N1-H/I	*Equus sp.*	M3 inf.	49.3	10.4	0.3
AA7-52.Y	AA7-52	N1-H/I	*Equus sp.*	M3 inf.	45.6	10.0	0.2
AA7-52.AB	AA7-52	N1-H/I	*Equus sp.*	M3 inf.	42.5	10.3	0.2
AA7-52.AE	AA7-52	N1-H/I	*Equus sp.*	M3 inf.	38.6	10.4	0.3
AA7-52.AH	AA7-52	N1-H/I	*Equus sp.*	M3 inf.	35.1	11.3	0.1
AA7-52.AK	AA7-52	N1-H/I	*Equus sp.*	M3 inf.	32.1	12.0	0.4
AA7-52.AN	AA7-52	N1-H/I	*Equus sp.*	M3 inf.	28.9	12.3	0.1

Sample ID	Tooth	Layer	Taxon	Tooth position	mm from ERJ	$\delta^{18}O$	SD
AA7-52.AQ	AA7-52	N1-H/I	*Equus sp.*	M3 inf.	25.8	12.1	0.3
AA7-52.AT	AA7-52	N1-H/I	*Equus sp.*	M3 inf.	22.8	11.4	0.2
AA7-52.AW	AA7-52	N1-H/I	*Equus sp.*	M3 inf.	19.5	11.4	0.1
AA7-52.AZ	AA7-52	N1-H/I	*Equus sp.*	M3 inf.	16.7	12.2	0.2
AA7-52.BC	AA7-52	N1-H/I	*Equus sp.*	M3 inf.	13.2	12.6	0.3
AA7-52.BF	AA7-52	N1-H/I	*Equus sp.*	M3 inf.	9.5	12.9	0.1
AA7-52.BH	AA7-52	N1-H/I	*Equus sp.*	M3 inf.	7.3	13.2	0.1
AA7-52.BJ	AA7-52	N1-H/I	*Equus sp.*	M3 inf.	5.0	13.2	0.3
AA8-334.A	AA8-334	N1-I	*Bos/Bison*	M2 sup.	20.8	12.8	0.3
AA8-334.D	AA8-334	N1-I	*Bos/Bison*	M2 sup.	17.4	12.3	0.1
AA8-334.G	AA8-334	N1-I	*Bos/Bison*	M2 sup.	14.1	11.8	0.0
AA8-334.J	AA8-334	N1-I	*Bos/Bison*	M2 sup.	11.1	11.8	0.1
AA8-334.M	AA8-334	N1-I	*Bos/Bison*	M2 sup.	7.9	11.0	0.6
AA8-334.P	AA8-334	N1-I	*Bos/Bison*	M2 sup.	5.3	10.7	0.3
AA8-334.S	AA8-334	N1-I	*Bos/Bison*	M2 sup.	2.5	9.9	0.1
CC7-2397.A	CC7-2397	N1-I/J	*Equus sp.*	M3 sup.	42.5	14.0	0.4
CC7-2397.D	CC7-2397	N1-I/J	*Equus sp.*	M3 sup.	38.3	13.8	0.4
CC7-2397.G	CC7-2397	N1-I/J	*Equus sp.*	M3 sup.	34.9	12.6	0.1
CC7-2397.J	CC7-2397	N1-I/J	*Equus sp.*	M3 sup.	31.8	11.6	0.3
CC7-2397.M	CC7-2397	N1-I/J	*Equus sp.*	M3 sup.	28.1	11.5	0.4
CC7-2397.P	CC7-2397	N1-I/J	*Equus sp.*	M3 sup.	24.1	12.1	0.1
CC7-2397.S	CC7-2397	N1-I/J	*Equus sp.*	M3 sup.	19.7	12.5	0.2
CC7-2397.V	CC7-2397	N1-I/J	*Equus sp.*	M3 sup.	15.9	13.4	0.1
CC7-2397.Y	CC7-2397	N1-I/J	*Equus sp.*	M3 sup.	13.0	13.2	0.2
CC7-2397.AB	CC7-2397	N1-I/J	*Equus sp.*	M3 sup.	9.7	12.4	0.5
CC7-2397.AE	CC7-2397	N1-I/J	*Equus sp.*	M3 sup.	6.5	11.4	0.3
CC7-2397.AH	CC7-2397	N1-I/J	*Equus sp.*	M3 sup.	3.3	12.0	0.1
CC7-2397.AJ	CC7-2397	N1-I/J	*Equus sp.*	M3 sup.	0.6	12.0	0.2
CC7-2478.A	CC7-2478	N1-J	*Equus sp.*	M3 sup.	60.7	14.4	0.1
CC7-2478.D	CC7-2478	N1-J	*Equus sp.*	M3 sup.	57.9	14.0	0.1
CC7-2478.G	CC7-2478	N1-J	*Equus sp.*	M3 sup.	54.3	13.3	0.2

Sample ID	Tooth	Layer	Taxon	Tooth position	mm from ERJ	$\delta^{18}O$	SD
CC7-2478.J	CC7-2478	N1-J	*Equus sp.*	M3 sup.	50.7	12.6	0.0
CC7-2478.M	CC7-2478	N1-J	*Equus sp.*	M3 sup.	46.7	12.2	0.2
CC7-2478.P	CC7-2478	N1-J	*Equus sp.*	M3 sup.	42.9	12.0	0.4
CC7-2478.S	CC7-2478	N1-J	*Equus sp.*	M3 sup.	38.8	12.3	0.2
CC7-2478.V	CC7-2478	N1-J	*Equus sp.*	M3 sup.	35.0	13.3	0.3
CC7-2478.Y	CC7-2478	N1-J	*Equus sp.*	M3 sup.	31.0	13.8	0.1
CC7-2478.AB	CC7-2478	N1-J	*Equus sp.*	M3 sup.	27.6	13.5	0.2
CC7-2478.AE	CC7-2478	N1-J	*Equus sp.*	M3 sup.	23.8	12.8	0.3
CC7-2478.AH	CC7-2478	N1-J	*Equus sp.*	M3 sup.	20.4	12.2	0.3
CC7-2478.AK	CC7-2478	N1-J	*Equus sp.*	M3 sup.	16.9	12.4	0.2
CC7-2478.AN	CC7-2478	N1-J	*Equus sp.*	M3 sup.	13.3	12.5	0.3
CC7-2478.AQ	CC7-2478	N1-J	*Equus sp.*	M3 sup.	9.5	14.5	0.1
CC7-2478.AT	CC7-2478	N1-J	*Equus sp.*	M3 sup.	6.6	14.6	0.2
CC7-2478.AW	CC7-2478	N1-J	*Equus sp.*	M3 sup.	3.1	13.1	0.2
CC7-2478.AY	CC7-2478	N1-J	*Equus sp.*	M3 sup.	0.5	13.6	0.2
CC7-2605.A	CC7-2605	N1-J	*Equus sp.*	P4 sup.	42.0	11.7	0.1
CC7-2605.D	CC7-2605	N1-J	*Equus sp.*	P4 sup.	37.6	11.9	0.2
CC7-2605.G	CC7-2605	N1-J	*Equus sp.*	P4 sup.	33.5	12.7	0.4
CC7-2605.J	CC7-2605	N1-J	*Equus sp.*	P4 sup.	29.5	14.8	0.3
CC7-2605.M	CC7-2605	N1-J	*Equus sp.*	P4 sup.	25.3	15.3	0.3
CC7-2605.P	CC7-2605	N1-J	*Equus sp.*	P4 sup.	21.8	16.4	0.1
CC7-2605.S	CC7-2605	N1-J	*Equus sp.*	P4 sup.	18.1	16.0	0.6
CC7-2605.V	CC7-2605	N1-J	*Equus sp.*	P4 sup.	14.7	15.5	
CC7-2605.Y	CC7-2605	N1-J	*Equus sp.*	P4 sup.	11.3	15.8	0.1
CC7-2605.AB	CC7-2605	N1-J	*Equus sp.*	P4 sup.	7.3	15.3	0.6
CC7-2605.AE	CC7-2605	N1-J	*Equus sp.*	P4 sup.	3.6	14.3	0.3
CC7-2605.AG	CC7-2605	N1-J	*Equus sp.*	P4 sup.	0.5	12.4	0.3
CC7-2813.A	CC7-2813	N1-I	*Equus sp.*	P2 sup.	59.0	11.9	0.2
CC7-2813.D	CC7-2813	N1-I	*Equus sp.*	P2 sup.	56.1	12.0	0.3
CC7-2813.G	CC7-2813	N1-I	*Equus sp.*	P2 sup.	53.4	12.3	0.3
CC7-2813.J	CC7-2813	N1-I	*Equus sp.*	P2 sup.	50.5	12.2	0.3

Sample ID	Tooth	Layer	Taxon	Tooth position	mm from ERJ	$\delta^{18}O$	SD
CC7-2813.M	CC7-2813	N1-I	*Equus sp.*	P2 sup.	47.4	13.2	0.3
CC7-2813.P	CC7-2813	N1-I	*Equus sp.*	P2 sup.	44.3	13.4	0.1
CC7-2813.S	CC7-2813	N1-I	*Equus sp.*	P2 sup.	41.0	13.1	0.0
CC7-2813.V	CC7-2813	N1-I	*Equus sp.*	P2 sup.	37.9	13.1	0.2
CC7-2813.Y	CC7-2813	N1-I	*Equus sp.*	P2 sup.	34.6	13.0	0.3
CC7-2813.AB	CC7-2813	N1-I	*Equus sp.*	P2 sup.	31.3	13.2	0.3
CC7-2813.AE	CC7-2813	N1-I	*Equus sp.*	P2 sup.	28.4	12.7	0.3
CC7-2813.AH	CC7-2813	N1-I	*Equus sp.*	P2 sup.	25.7	12.8	0.3
CC7-2813.AK	CC7-2813	N1-I	*Equus sp.*	P2 sup.	22.8	12.5	0.3
CC7-2813.AN	CC7-2813	N1-I	*Equus sp.*	P2 sup.	19.3	12.6	0.1
CC7-2813.AQ	CC7-2813	N1-I	*Equus sp.*	P2 sup.	15.9	13.1	0.2
CC7-2813.AT	CC7-2813	N1-I	*Equus sp.*	P2 sup.	12.1	13.3	0.3
CC7-2813.AW	CC7-2813	N1-I	*Equus sp.*	P2 sup.	9.2	13.3	0.3
CC7-2813.AZ	CC7-2813	N1-I	*Equus sp.*	P2 sup.	6.0	13.4	0.1
CC7-2813.BB	CC7-2813	N1-I	*Equus sp.*	P2 sup.	3.8	13.5	0.4
CC7-2813.BF	CC7-2813	N1-I	*Equus sp.*	P2 sup.	0.4	14.0	0.4
CC7-3018.A	CC7-3018	N1-K	*Equus sp.*	P3 sup.	55.7	13.8	0.5
CC7-3018.D	CC7-3018	N1-K	*Equus sp.*	P3 sup.	52.0	12.7	0.2
CC7-3018.G	CC7-3018	N1-K	*Equus sp.*	P3 sup.	48.2	13.8	0.6
CC7-3018.J	CC7-3018	N1-K	*Equus sp.*	P3 sup.	45.0	13.6	0.3
CC7-3018.M	CC7-3018	N1-K	*Equus sp.*	P3 sup.	41.2	13.9	0.0
CC7-3018.P	CC7-3018	N1-K	*Equus sp.*	P3 sup.	38.3	14.0	0.2
CC7-3018.S	CC7-3018	N1-K	*Equus sp.*	P3 sup.	34.7	14.3	0.2
CC7-3018.V	CC7-3018	N1-K	*Equus sp.*	P3 sup.	31.2	14.5	0.1
CC7-3018.Y	CC7-3018	N1-K	*Equus sp.*	P3 sup.	27.6	14.3	0.3
CC7-3018.AB	CC7-3018	N1-K	*Equus sp.*	P3 sup.	24.1	13.9	0.2
CC7-3018.AE	CC7-3018	N1-K	*Equus sp.*	P3 sup.	20.7	13.4	0.1
CC7-3018.AH	CC7-3018	N1-K	*Equus sp.*	P3 sup.	17.1	13.0	0.1
CC7-3018.AK	CC7-3018	N1-K	*Equus sp.*	P3 sup.	13.8	13.2	0.2
CC7-3018.AN	CC7-3018	N1-K	*Equus sp.*	P3 sup.	10.5	13.7	0.2
CC7-3018.AQ	CC7-3018	N1-K	*Equus sp.*	P3 sup.	6.9	13.6	0.3

Sample ID	Tooth	Layer	Taxon	Tooth position	mm from ERJ	$\delta^{18}O$	SD
CC7-3018.AT	CC7-3018	N1-K	*Equus sp.*	P3 sup.	2.5	12.4	0.3
CC7-3018.AU	CC7-3018	N1-K	*Equus sp.*	P3 sup.	0.8	12.7	0.2
CC8-18.A	CC8-18	N1-I	*Bos/Bison*	M3 inf.	39.0	11.8	0.2
CC8-18.D	CC8-18	N1-I	*Bos/Bison*	M3 inf.	36.0	11.3	0.2
CC8-18.G	CC8-18	N1-I	*Bos/Bison*	M3 inf.	33.1	11.3	0.4
CC8-18.J	CC8-18	N1-I	*Bos/Bison*	M3 inf.	29.5	11.1	0.4
CC8-18.M	CC8-18	N1-I	*Bos/Bison*	M3 inf.	26.8	11.2	0.3
CC8-18.P	CC8-18	N1-I	*Bos/Bison*	M3 inf.	23.7	12.3	0.2
CC8-18.S	CC8-18	N1-I	*Bos/Bison*	M3 inf.	20.7	11.8	0.5
CC8-18.V	CC8-18	N1-I	*Bos/Bison*	M3 inf.	17.9	12.4	0.2
CC8-18.Y	CC8-18	N1-I	*Bos/Bison*	M3 inf.	15.1	13.0	0.1
CC8-18.AB	CC8-18	N1-I	*Bos/Bison*	M3 inf.	12.0	12.5	0.4
CC8-18.AE	CC8-18	N1-I	*Bos/Bison*	M3 inf.	9.3	12.7	0.2
CC8-18.AH	CC8-18	N1-I	*Bos/Bison*	M3 inf.	6.4	11.9	0.4
CC8-18.AK	CC8-18	N1-I	*Bos/Bison*	M3 inf.	3.3	11.3	0.4
CC8-2419.A	CC8-2419	N1-K	*Equus sp.*	M3 sup.	49.5	13.6	0.3
CC8-2419.D	CC8-2419	N1-K	*Equus sp.*	M3 sup.	46.1	14.1	0.2
CC8-2419.G	CC8-2419	N1-K	*Equus sp.*	M3 sup.	43.6	13.7	0.3
CC8-2419.J	CC8-2419	N1-K	*Equus sp.*	M3 sup.	41.3	13.9	0.1
CC8-2419.M	CC8-2419	N1-K	*Equus sp.*	M3 sup.	38.4	14.3	0.1
CC8-2419.P	CC8-2419	N1-K	*Equus sp.*	M3 sup.	35.6	14.3	0.3
CC8-2419.S	CC8-2419	N1-K	*Equus sp.*	M3 sup.	32.3	14.6	0.3
CC8-2419.V	CC8-2419	N1-K	*Equus sp.*	M3 sup.	29.7	14.6	0.4
CC8-2419.Y	CC8-2419	N1-K	*Equus sp.*	M3 sup.	26.3	14.2	0.5
CC8-2419.AB	CC8-2419	N1-K	*Equus sp.*	M3 sup.	23.2	13.6	0.1
CC8-2419.AE	CC8-2419	N1-K	*Equus sp.*	M3 sup.	20.2	13.5	0.3
CC8-2419.AH	CC8-2419	N1-K	*Equus sp.*	M3 sup.	17.2	13.6	0.3
CC8-2419.AK	CC8-2419	N1-K	*Equus sp.*	M3 sup.	13.1	13.3	0.3
CC8-2419.AN	CC8-2419	N1-K	*Equus sp.*	M3 sup.	10.9	13.6	0.3
CC8-2419.AQ	CC8-2419	N1-K	*Equus sp.*	M3 sup.	7.7	13.7	0.4
CC8-2419.AT	CC8-2419	N1-K	*Equus sp.*	M3 sup.	4.9	13.3	0.2

Sample ID	Tooth	Layer	Taxon	Tooth position	mm from ERJ	$\delta^{18}O$	SD
CC8-2419.AW	CC8-2419	N1-K	*Equus sp.*	M3 sup.	1.7	12.7	0.0

Table S3: Strontium isotope data genertated in this study. Analyses were conducted for a subset of sequential tooth enamel samples and used to assess *Equus sp.* and *Bos/Bison* migratory behaviour.

Sample ID	Layer	$^{87/86}Sr$	Concentration (ppm)
AA7-121.U	N1-H/I	0.7092173	152
AA7-121.D	N1-H/I	0.7094012	146
AA7-52.AN	N1-H/I	0.7092226	223
AA7-52.Y	N1-H/I	0.7094083	238
CC7-2813.P	N1-I	0.7096933	237
CC7-2813.AK	N1-I	0.7095664	243
CC8-18.Y	N1-I	0.7092169	245
CC8-18.J	N1-I	0.7092192	224
CC7-2397.V.U	N1-I/J	0.7089614	282
CC7-2397.M.N	N1-I/J	0.7089819	267
CC7-2478.AB	N1-J	0.7092533	227
CC7-2478.P	N1-J	0.7092065	316
CC7-3018.AQ	N1-K	0.7093196	220
CC7-3018.D	N1-K	0.7094102	234
CC8-2419.AN	N1-K	0.7093264	227
CC8-2419.AE	N1-K	0.7092620	218

REFERENCES AND NOTES

1. M. Staubwasser, V. Draguşin, B. P. Onac, S. Assonov, V. Ersek, D. L. Hoffmann, D. Veres, Impact of climate change on the transition of Neanderthals to modern humans in Europe. *Proc. Natl. Acad. Sci.* **115**, 9116–9121 (2018).

2. U. C. Müller, J. Pross, P. C. Tzedakis, C. Gamble, U. Kotthoff, G. Schmiedl, S. Wulf, K. Christanis, The role of climate in the spread of modern humans into Europe. *Quat. Sci. Rev.* **30**, 273–279 (2011).

3. J. J. Hublin, The modern human colonization of western Eurasia: When and where? *Quat. Sci. Rev.* **118**, 194–210 (2015).

4. S. L. Kuhn, N. Zwyns, Rethinking the initial Upper Paleolithic. *Quat. Int.* **347**, 29–38 (2014).

5. J.-J. Hublin, N. Sirakov, V. Aldeias, S. Bailey, E. Bard, V. Delvigne, E. Endarova, Y. Fagault, H. Fewlass, M. Hajdinjak, B. Kromer, I. Krumov, J. Marreiros, N. L. Martisius, L. Paskulin, V. Sinet-Mathiot, M. Meyer, S. Pääbo, V. Popov, Z. Rezek, S. Sirakova, M. M. Skinner, G. M. Smith, R. Spasov, S. Talamo, T. Tuna, L. Wacker, F. Welker, A. Wilcke, N. Zahariev, S. P. McPherron, T. Tsanova, Initial upper palaeolithic *Homo sapiens* from bacho Kiro Cave, Bulgaria. *Nature* **581**, 299–302 (2020).

6. H. Fewlass, S. Talamo, L. Wacker, B. Kromer, T. Tuna, Y. Fagault, E. Bard, S. P. McPherron, V. Aldeias, R. Maria, N. L. Martisius, L. Paskulin, Z. Rezek, V. Sinet-Mathiot, S. Sirakova, G. M. Smith, R. Spasov, F. Welker, N. Sirakov, T. Tsanova, J. J. Hublin, A 14C chronology for the Middle to Upper Palaeolithic transition at Bacho Kiro Cave, Bulgaria. *Nat. Ecol. Evol.* **4**, 794–801 (2020).

7. P. J. Reimer, W. E. N. Austin, E. Bard, A. Bayliss, P. G. Blackwell, C. B. Ramsey, M. Butzin, H. Cheng, R Lawrence Edwards, M. Friedrich, P. M. Grootes, T. P. Guilderson, I. Hajdas, T. J. Heaton, A. G. Hogg, K. A. Hughen, B. Kromer, S. W. Manning, R. Muscheler, J. G. Palmer, C. Pearson, J. van der Plicht, R. W. Reimer, D. A. Richards, E Marian Scott, J. R. Southon, C. S. M. Turney, L. Wacker, F. Adolphi, U. Büntgen, M. Capano, S. M. Fahrni, A. Fogtmann-Schulz, R. Friedrich, P. Köhler, S. Kudsk, F. Miyake, J. Olsen, The IntCal20 Northern Hemisphere radiocarbon age calibration curve (0-55 cal kBP). *Radiocarbon* **62**, 725–757 (2020).

8. Q. Fu, M. Hajdinjak, O. T. Moldovan, S. Constantin, S. Mallick, P. Skoglund, N. Patterson, N. Rohland, I. Lazaridis, B. Nickel, B. Viola, K. Prüfer, M. Meyer, J. Kelso, D. Reich, S. Pääbo, An early modern human from Romania with a recent Neanderthal ancestor. *Nature* **524**, 216–219 (2015).

9. Q. Fu, C. Posth, M. Hajdinjak, M. Petr, S. Mallick, D. Fernandes, A. Furtwängler, W. Haak, M. Meyer, A. Mittnik, B. Nickel, A. Peltzer, N. Rohland, V. Slon, S. Talamo, I. Lazaridis, M. Lipson, I. Mathieson, S. Schiffels, P. Skoglund, A. P. Derevianko, N. Drozdov, V. Slavinsky, A. Tsybankov, R. G. Cremonesi, F. Mallegni, B. Gély, E. Vacca, M. R. G. Morales, L. G. Straus, C. Neugebauer-Maresch, M. Teschler-Nicola, S. Constantin, O. T. Moldovan, S. Benazzi, M. Peresani, D. Coppola, M. Lari, S. Ricci, A. Ronchitelli, F. Valentin, C. Thevenet, K. Wehrberger, D. Grigorescu, H. Rougier, I. Crevecoeur, D. Flas, P. Semal, M. A. Mannino, C. Cupillard, H. Bocherens, N. J. Conard, K. Harvati, V. Moiseyev, D. G. Drucker, J. Svoboda, M. P. Richards, D. Caramelli, R. Pinhasi, J. Kelso, N. Patterson, J. Krause, S. Pääbo, D. Reich, The genetic history of Ice Age Europe. *Nature* **534**, 200–205 (2016).

10. J. K. Kozłowski, B. Ginter, *Excavation in the Bacho Kiro Cave (Bulgaria). Final report* (Państwowe Wydawnictwo Naukowe, 1982).

11. V. V. Popov, in *The Pleistocene: Geography, GEOLOGY, and Fauna*, G. Huard, J. Gareau, Eds. (2018), pp. 109–236.

12. Z. Chen, A. S. Auler, M. Bakalowicz, D. Drew, F. Griger, J. Hartmann, G. Jiang, N. Moosdorf, A. Richts, Z. Stevanovic, G. Veni, N. Goldscheider, The World Karst Aquifer Mapping project: Concept, mapping procedure and map of Europe. *Hydrogeol. J.* **25**, 771–785 (2017).

13. L. Scherler, T. Tütken, D. Becker, Carbon and oxygen stable isotope compositions of late Pleistocene mammal teeth from dolines of Ajoie (Northwestern Switzerland). *Quat. Res.* **82**, 378–387 (2014).

14. D. Pushkina, H. Bocherens, R. Ziegler, Unexpected palaeoecological features of the Middle and Late Pleistocene large herbivores in southwestern Germany revealed by stable isotopic abundances in tooth enamel. *Quat. Int.* **339-340**, 164–178 (2014).

15. L. M. Arppe, J. A. Karhu, Oxygen isotope values of precipitation and the thermal climate in Europe during the middle to late Weichselian ice age. *Quat. Sci. Rev.* **29**, 1263–1275 (2010).

16. G. J. Bowen, J. Revenaugh, Interpolating the isotopic composition of modern meteoric precipitation. *Water Resour. Res.* **39**, 1299 (2003).

17. G. J. Bowen, L. I. Wassenaar, K. A. Hobson, Global application of stable hydrogen and oxygen isotopes to wildlife forensics. *Oecologia* **143**, 337–348 (2005).

18. IAEA/WMO, Global Network of Isotopes in Precipitation. The GNIP Database (2020); https://nucleus.iaea.org/wiser.

19. I. Obreht, C. Zeeden, U. Hambach, D. Veres, S. B. Marković, J. Bösken, Z. Svirčev, N. Bačević, M. B. Gavrilov, F. Lehmkuhl, Tracing the influence of Mediterranean climate on Southeastern Europe during the past 350,000 years. *Sci. Rep.* **6**, 36334 (2016).

20. A. Wegwerth, A. Ganopolski, G. Ménot, J. Kaiser, O. Dellwig, E. Bard, F. Lamy, H. W. Arz, Black Sea temperature response to glacial millennial-scale climate variability. *Geophys. Res. Lett.* **42**, 8147–8154 (2015).

21. A. Feurdean, A. Perşoiu, I. Tanţău, T. Stevens, E. K. Magyari, B. P. Onac, S. Marković, M. Andrič, S. Connor, S. Fărcaş, M. Gałka, T. Gaudeny, W. Hoek, P. Kolaczek, P. Kuneš, M. Lamentowicz, E. Marinova, D. J. Michczyńska, I. Perşoiu, M. Płóciennik, M. Słowiński, M. Stancikaite, P. Sumegi, A. Svensson, T. Tămaş, A. Timar, S. Tonkov, M. Toth, S. Veski, K. J. Willis, V. Zernitskaya, Climate variability and associated vegetation response throughout Central and Eastern Europe (CEE) between 60 and 8ka. *Quat. Sci. Rev.* **106**, 206–224 (2014).

22. E. Kjellström, J. Brandefelt, J. O. Näslund, B. Smith, G. Strandberg, A. H. L. Voelker, B. Wohlfarth, Simulated climate conditions in Europe during the Marine Isotope Stage 3 stadial. *Boreas* **39**, 436–456 (2010).

23. N. Zwyns, C. H. Paine, B. Tsedendorj, S. Talamo, K. E. Fitzsimmons, A. Gantumur, L. Guunii, O. Davakhuu, D. Flas, T. Dogandžić, N. Doerschner, F. Welker, J. C. Gillam, J. B. Noyer, R. S. Bakhtiary, A. F. Allshouse, K. N. Smith, A. M. Khatsenovich, E. P. Rybin, G. Byambaa, J. J.

Hublin, The Northern route for human dispersal in central and northeast asia: New evidence from the site of Tolbor-16, Mongolia. *Sci. Rep.* **9**, 11759 (2019).

24. D. Mihailović, Push-and-pull factors of the Middle to Upper Paleolithic transition in the Balkans. *Quat. Int.* **551**, 47–62 (2020).

25. P. R. Nigst, P. Haesaerts, F. Damblon, C. Frank-Fellner, C. Mallol, B. Viola, M. Götzinger, L. Niven, G. Trnka, J.-J. Hublin, Early modern human settlement of Europe north of the Alps occurred 43,500 years ago in a cold steppe-type environment. *Proc. Natl. Acad. Sci. U.S.A.* **111**, 14394–14399 (2014).

26. D. Richter, G. Tostevin, P. Škrdla, W. Davies, New radiometric ages for the Early Upper Palaeolithic type locality of Brno-Bohunice (Czech Republic): Comparison of OSL, IRSL, TL and 14C dating results. *J. Archaeol. Sci.* **36**, 708–720 (2009).

27. N. Zwyns, thesis, Leiden University (2012).

28. W. Davies, P. Gollop, The human presence in Europe during the Last Glacial Period II. Climate tolerance and climate preferences of Mid-and Late Glacial hominids, in *Neanderthals and Modern Humans in the European Landscape of the Last Glaciation* (The McDonald Institute for Archaeological Research, 2003), pp. 131–146.

29. S. Constantin, A. V. Bojar, S. E. Lauritzen, J. Lundberg, Holocene and Late Pleistocene climate in the sub-Mediterranean continental environment: A speleothem record from Poleva Cave (Southern Carpathians, Romania). *Palaeogeogr. Palaeoclimatol. Palaeoecol.* **243**, 322–338 (2007).

30. D. L. Dettman, M. J. Kohn, J. Quade, F. J. Ryerson, T. P. Ojha, S. Hamidullah, Seasonal stable isotope evidence for a strong Asian monsoon throughout the past 10.7 m.y. *Geology* **29**, 31–34 (2001).

31. T. Tütken, T. W. Vennemann, H. Janz, E. P. J. Heizmann, Palaeoenvironment and palaeoclimate of the Middle Miocene lake in the Steinheim basin, SW Germany: A reconstruction from C, O, and Sr isotopes of fossil remains. *Palaeogeogr. Palaeoclimatol. Palaeoecol.* **241**, 457–491 (2006).

32. K. Britton, B. T. Fuller, T. Tütken, S. Mays, M. P. Richards, Oxygen isotope analysis of human bone phosphate evidences weaning age in archaeological populations. *Am. J. Phys. Anthropol.* **157**, 226–241 (2015).

33. W. A. Brand, T. B. Coplen, A. T. Aerts-Bijma, J. K. Böhlke, M. Gehre, H. Geilmann, M. Gröning, H. G. Jansen, H. A. J. Meijer, S. J. Mroczkowski, H. Qi, K. Soergel, H. Stuart-Williams, S. M. Weise, R. A. Werner, Comprehensive inter-laboratory calibration of reference materials for δ^{18}O versus VSMOW using various on-line high-temperature conversion techniques. *Rapid Commun. Mass Spectrom.* **23**, 999–1019 (2009).

34. E. Pucéat, M. M. Joachimski, A. Bouilloux, F. Monna, A. Bonin, S. Motreuil, P. Morinière, S. Hénard, J. Mourin, G. Dera, D. Quesne, Revised phosphate-water fractionation equation reassessing paleotemperatures derived from biogenic apatite. *Earth Planet. Sci. Lett.* **298**, 135–142 (2010).

35. S. R. Copeland, M. Sponheimer, P. J. le Roux, V. Grimes, J. A. Lee-Thorp, D. J. de Ruiter, M. P. Richards, Strontium isotope ratios (^{87}Sr/^{86}Sr) of tooth enamel: A comparison of solution and laser ablation multicollector inductively coupled plasma mass spectrometry methods. *Rapid Commun. Mass Spectrom.* **22**, 3187–3194 (2008).

36. C. M. Johnson, C. J. Fridrich, Non-monotonic chemical and O, Sr, Nd, and Pb isotope zonations and heterogeneity in the mafic- to silicic-composition magma chamber of the Grizzly Peak Tuff, Colorado. *Contrib. Mineral. Petrol.* **105**, 677–690 (1990).

37. A. J. E. Pryor, R. E. Stevens, T. C. O'Connell, J. R. Lister, Quantification and propagation of errors when converting vertebrate biomineral oxygen isotope data to temperature for palaeoclimate reconstruction. *Palaeogeogr. Palaeoclimatol. Palaeoecol.* **412**, 99–107 (2014).

38. B. H. Passey, T. E. Cerling, G. T. Schuster, T. F. Robinson, B. L. Roeder, S. K. Krueger, Inverse methods for estimating primary input signals from time-averaged isotope profiles. *Geochim. Cosmochim. Acta* **69**, 4101–4116 (2005).

39. R Core Team, *R: A Language and Environment for Statistical Computing* (R Foundation for Statistical Computing, Vienna, Austria, 2020; https://r-project.org/).

40. J. Allaire, J. Cheng, Y. Xie, J. McPherson, W. Chang, J. Allen, R. Hyndman, rmarkdown: Dynamic documents for R (R package version 1.0) (2018).

41. N. Center Aviation Weather, Gorna Oryahovitsa airport (LBGO) METAR (2012–2020) (2020); https://aviationweather.gov/metar.

42. K. A. Hoppe, S. M. Stover, J. R. Pascoe, R. Amundson, Tooth enamel biomineralization in extant horses: Implications for isotopic microsampling. *Palaeogeogr. Palaeoclimatol. Palaeoecol.* **206**, 355–365 (2004).

43. C. Gadbury, L. Todd, A. H. Jahren, R. Amundson, Spatial and temporal variations in the isotopic composition of bison tooth enamel from the Early Holocene Hudson-Meng Bone Bed, Nebraska. *Palaeogeogr. Palaeoclimatol. Palaeoecol.* **157**, 79–93 (2000).

44. D. A. E. Garrod, B. Howe, J. H. Gaul, Excavations in the cave of Bacho Kiro, north-east Bulgaria. *Bulletin of the American School of Prehistoric Research.* **15**, 46–126 (1939).

45. C. Bronk Ramsey, Bayesian analysis of radiocarbon dates. *Radiocarbon* **51**, 337–360 (2009).

46. M. J. Aitken, *Introduction to Optical Dating: The Dating of Quaternary Sediments by the Use of Photon-stimulated Luminescence* (Clarendon Press, 1998).

47. J. Buylaert, M. Jain, A. S. Murray, K. J. Thomsen, C. Thiel, R. Sohbati, A robust feldspar luminescence dating method for Middle and Late Pleistocene sediments. *Boreas* **41**, 435–451 (2012).

48. J.-P. Buylaert, A. S. Murray, K. J. Thomsen, M. Jain, Testing the potential of an elevated temperature IRSL signal from K-feldspar. *Radiat. Meas.* **44**, 560–565 (2009).

49. C. Thiel, J.-P. Buylaert, A. Murray, B. Terhorst, I. Hofer, S. Tsukamoto, M. Frechen, Luminescence dating of the Stratzing loess profile (Austria)—Testing the potential of an elevated temperature post-IR IRSL protocol. *Quat. Int.* **234**, 23–31 (2011).

50. K. J. Thomsen, A. S. Murray, M. Jain, L. Bøtter-Jensen, Laboratory fading rates of various luminescence signals from feldspar-rich sediment extracts. *Radiat. Meas.* **43**, 1474–1486 (2008).

51. D. J. Huntley, M. Lamothe, Ubiquity of anomalous fading in K-feldspars and the measurement and correction for it in optical dating. *Can. J. Earth Sci.* **38**, 1093–1106 (2001).

52. S. Kreutzer, C. Schmidt, R. DeWitt, M. Fuchs, The a-value of polymineral fine grain samples measured with the post-IR IRSL protocol. *Radiat. Meas.* **69**, 18–29 (2014).

53. I. D. Clark, P. Fritz, *Environmental Isotopes in Hydrogeology* (Lewis Publishers, 1997).

54. K. Rozanski, L. Araguás-Araguás, R. Gonfiantini, Isotopic patterns in modern global precipitation. *Clim. Chang. Cont.* **78**, 1–36 (1993).

55. S. Müller, C. Stumpp, J. H. Sørensen, S. Jessen, Spatiotemporal variation of stable isotopic composition in precipitation: Post-condensational effects in a humid area. *Hydrol. Process.* **31**, 3146–3159 (2017).

56. C. Stumpp, J. Klaus, W. Stichler, Analysis of long-term stable isotopic composition in German precipitation. *J. Hydrol.* **517**, 351–361 (2014).

57. W. Dansgaard, Stable isotopes in precipitation. *Tellus* **16**, 436–468 (1964).

58. M. J. Kohn, J. M. Welker, On the temperature correlation of δ^{18}O in modern precipitation. *Earth Planet. Sci. Lett.* **231**, 87–96 (2005).

59. M. J. Kohn, M. J. Schoeninger, J. W. Valley, Herbivore tooth oxygen isotope compositions: Effects of diet and physiology. *Geochim. Cosmochim. Acta* **60**, 3889–3896 (1996).

60. B. Luz, Y. Kolodny, M. Horowitz, Fractionation of oxygen isotopes between mammalian bone-phosphate and environmental drinking water. *Geochim. Cosmochim. Acta* **48**, 1689–1693 (1984).

61. A. Longinelli, Oxygen isotopes in mammal bone phosphate: A new tool for paleohydrological and paleoclimatological research? *Geochim. Cosmochim. Acta* **48**, 385–390 (1984).

62. P. Iacumin, H. Bocherens, Oxygen isotope analyses of co-existing carbonate and phosphate in biogenic apatite: A way to monitor diagenetic alteration of bone phosphate? *Earth Planet. Sci. Lett.* **142**, 1–6 (1996).

63. T. Tütken, H. Furrer, T. Walter Vennemann, Stable isotope compositions of mammoth teeth from Niederweningen, Switzerland: Implications for the Late Pleistocene climate, environment, and diet. *Quat. Int.* **164-165**, 139–150 (2007).

64. G. Skrzypek, R. Sadler, A. Wiśniewski, Reassessment of recommendations for processing mammal phosphate δ18O data for paleotemperature reconstruction. *Palaeogeogr. Palaeoclimatol. Palaeoecol.* **446**, 162–167 (2016).

65. K. A. Hoppe, Correlation between the oxygen isotope ratio of North American bison teeth and local waters: Implication for paleoclimatic reconstructions. *Earth Planet. Sci. Lett.* **244**, 408–417 (2006).

66. K. Rozanski, L. Araguás-Araguás, R. Gonfiantini, Relation between long-term trends of oxygen-18 isotope composition of precipitation and climate. *Science* **258**, 981–985 (1992).

67. S. Pederzani, K. Britton, Oxygen isotopes in bioarchaeology: Principles and applications, challenges and opportunities. *Earth Sci. Rev.* **188**, 77–107 (2019).

68. G. M. O. Maloiy, Water metabolism of East African ruminants in arid and semi-arid regions. *Z. Tierzuecht. Zuechtungsbiol.* **90**, 219–228 (1973).

69. R. A. Arias, T. L. Mader, Environmental factors affecting daily water intake on cattle finished in feedlots. *J. Anim. Sci.* **89**, 245–251 (2011).

70. T. McHugh, Social behavior of the American buffalo (*Bison bison bison*). *Fortschr. Zool.* **43**, 1–40 (1958).

71. C. F. Winchester, M. J. Morris, Water intake rates of cattle. *J. Anim. Sci.* **15**, 722–740 (1956).

72. S. Groenendyk, P. B. English, I. Abetz, External balance of water and electrolytes in the horse. *Equine Vet. J.* **20**, 189–193 (1988).

73. K. M. Scheibe, K. Eichhorn, B. Kalz, W. J. Streich, A. Scheibe, Water consumption and watering behavior of Przewalski horses (*Equus ferus przewalskii*) in a semireserve. *Zoo Biol.* **17**, 181–192 (1998).

74. K. A. Houpt, A. Eggleston, K. Kunkle, T. R. Houpt, Effect of water restriction on equine behaviour and physiology. *Equine Vet. J.* **32**, 341–344 (2000).

75. M. Hinton, On the watering of horses: A review. *Equine Vet. J.* **10**, 27–31 (1978).

76. D. D'Angela, A. Longinelli, Oxygen isotopes in living mammal's bone phosphate: Further results. *Chem. Geol.* **86**, 75–82 (1990).

77. J. D. Bryant, B. Luz, P. N. Froelich, Oxygen isotopic composition of fossil horse tooth phosphate as a record of continental paleoclimate. *Palaeogeogr. Palaeoclimatol. Palaeoecol.* **107**, 303–316 (1994).

78. J. D. Bryant, P. N. Froelich, W. J. Showers, B. J. Genna, A tale of two quarries: Biologic and taphonomic signatures in the oxygen isotope composition of tooth enamel phosphate from modern and Miocene equids. *Palaios* **11**, 397–408 (1996).

79. K. A. Hoppe, R. Amundson, M. Vavra, M. P. McClaran, D. L. Anderson, Isotopic analysis of tooth enamel carbonate from modern North American feral horses: Implications for paleoenvironmental reconstructions. *Palaeogeogr. Palaeoclimatol. Palaeoecol.* **203**, 299–311 (2004).

80. B. Sánchez Chillón, M. T. Alberdi, G. Leone, F. P. Bonadonna, B. Stenni, A. Longinelli, Oxygen isotopic composition of fossil equid tooth and bone phosphate: An archive of difficult interpretation. *Palaeogeogr. Palaeoclimatol. Palaeoecol.* **107**, 317–328 (1994).

81. J. R. Gat, *Isotope Hydrology: A Study of the Water Cycle* (Imperila College Press, 2010), vol. 6 of *Series on Environmental Science and Management*.

82. W. G. Darling, A. H. Bath, J. C. Talbot, The O & H stable isotopic composition of fresh waters in the British Isles. 2. Surface waters and groundwater. *Hydrol. Earth Syst. Sci.* **7**, 183–195 (2003).

83. J. Halder, S. Terzer, L. I. Wassenaar, L. Araguás-Araguás, P. K. Aggarwal, The Global Network of Isotopes in Rivers (GNIR): Integration of water isotopes in watershed observation and riverine research. *Hydrol. Earth Syst. Sci.* **19**, 3419–3431 (2015).

84. R. Gonfiantini, Environmental isotopes in lake studies, in *Handbook of Environmental Isotope Geochemistry; The Terrestrial Environment* (1986), pp. 113–168.

85. Bulgarian Academy of Sciences, Dryanovska river, in *Golyama entsiklopediya—Bulgaria* (2012), pp. 1870–1871.

86. E. Bojilova, Inter-annual distribution for Yantra river basin, North Bulgaria. *18 Conference of the Danubian Countries on Hydrological Forcasting and Hydrological Bases of Water Management* (2017).

87. G. J. Bowen, OIPC: The online isotopes in precipitation calculator, version 3.1 (2020); http://waterisotopes.org.

88. N. M. Kortelainen, J. A. Karhu, Regional and seasonal trends in the oxygen and hydrogen isotope ratios of Finnish groundwaters: A key for mean annual precipitation. *J. Hydrol.* **285**, 143–157 (2004).

89. K. Rozanski, Deuterium and oxygen-18 in European groundwaters—Links to atmospheric circulation in the past. *Chem. Geol.* **52**, 349–363 (1985).

90. R. van Geldern, A. Baier, H. L. Subert, S. Kowol, L. Balk, J. A. C. Barth, Pleistocene paleo-groundwater as a pristine fresh water resource in southern Germany—Evidence from stable and radiogenic isotopes. *Sci. Total Environ.* **496**, 107–115 (2014).

91. P. K. Aggarwal, O. A. Alduchov, K. O. Froehlich, L. Araguás-Araguás, N. C. Sturchio, N. Kurita, Stable isotopes in global precipitation: A unified interpretation based on atmospheric moisture residence time. *Geophys. Res. Lett.* **39**, L11705 (2012).

92. G. J. Bowen, J. B. West, in *Tracking Animal Migration with Stable Isotopes*, K. A. Hobson, L. I. Wassenaar, Eds. (Elsevier, 2008), vol. 2 of *Terrestrial Ecology*, pp. 79–105.

93. P. D. Akers, J. M. Welker, G. A. Brook, Reassessing the role of temperature in precipitation oxygen isotopes across the eastern and central United States through weekly precipitation-day data. *Water Resour. Res.* **53**, 7644–7661 (2017).

94. G. A. Schmidt, G. Hoffmann, D. T. Shindell, Y. Hu, Modeling atmospheric stable water isotopes and the potential for constraining cloud processes and stratosphere-troposphere water exchange. *J. Geophys. Res.-Atmos.* **110**, D21314 (2005).

95. A. Zuber, S. M. Weise, J. Motyka, K. Osenbrück, K. Rózański, Age and flow pattern of groundwater in a Jurassic limestone aquifer and related Tertiary sands derived from combined isotope, noble gas and chemical data. *J. Hydrol.* **286**, 87–112 (2004).

96. F. Kaspar, N. Kühl, U. Cubasch, T. Litt, A model-data comparison of European temperatures in the Eemian interglacial. *Geophys. Res. Lett.* **32**, L11703 (2005).

97. G. Skrzypek, A. Winiewski, P. F. Grierson, How cold was it for Neanderthals moving to Central Europe during warm phases of the last glaciation? *Quat. Sci. Rev.* **30**, 481–487 (2011).

98. K. Britton, V. Grimes, L. Niven, T. E. Steele, S. J. P. McPherron, M. Soressi, T. E. Kelly, J. Jaubert, J.-J. Hublin, M. P. Richards, Strontium isotope evidence for migration in late Pleistocene Rangifer: Implications for Neanderthal hunting strategies at the Middle Palaeolithic site of Jonzac, France. *J. Hum. Evol.* **61**, 176–185 (2011).

99. M. C. Dean, Growth layers and incremental markings in hard tissues; a review of the literature and some preliminary observations about enamel structure in *Paranthropus boisei*. *J. Hum. Evol.* **16**, 157–172 (1987).

100. S. Hillson, *Teeth* (Cambridge, 2012).

101. H. C. Fricke, J. R. O'Neil, Inter- and intra-tooth variation in the oxygen isotope composition of mammalian tooth enamel phosphate: Implications for palaeoclimatological and palaeobiological research. *Palaeogeogr. Palaeoclimatol. Palaeoecol.* **126**, 91–99 (1996).

102. H. C. Fricke, W. C. Clyde, J. R. O'Neil, Intra-tooth variations in δ^{18}O(PO4) of mammalian tooth enamel as a record of seasonal variations in continental climate variables. *Geochim. Cosmochim. Acta* **62**, 1839–1850 (1998).

103. S. A. Blumenthal, T. E. Cerling, K. L. Chritz, T. G. Bromage, R. Kozdon, J. W. Valley, Stable isotope time-series in mammalian teeth: In situ δ^{18}O from the innermost enamel layer. *Geochim. Cosmochim. Acta* **124**, 223–236 (2014).

104. M. Balasse, Reconstructing dietary and environmental history from enamel isotopic analysis: Time resolution of intra-tooth sequential sampling. *Int. J. Osteoarchaeol.* **12**, 155–165 (2002).

105. D. R. Green, G. M. Green, A. S. Colman, F. B. Bidlack, P. Tafforeau, T. M. Smith, Synchrotron imaging and Markov Chain Monte Carlo reveal tooth mineralization patterns. *PLOS ONE* **12**, e0186391 (2017).

106. M. J. Kohn, Comment: Tooth enamel mineralization in ungulates: Implications for recovering a primary isotopic time-series, by B. H. Passey and T. E. Cerling (2002). *Geochim. Cosmochim. Acta* **68**, 403–405 (2004).

107. B. H. Passey, T. E. Cerling, Tooth enamel mineralization in ungulates: Implications for recovering a primary isotopic time-series. *Geochim. Cosmochim. Acta* **66**, 3225–3234 (2002).

108. R. B. Trayler, M. J. Kohn, Tooth enamel maturation reequilibrates oxygen isotope compositions and supports simple sampling methods. *Geochim. Cosmochim. Acta* **198**, 32–47 (2016).

109. R. Bendrey, D. Vella, A. Zazzo, M. Balasse, S. Lepetz, Exponentially decreasing tooth growth rate in horse teeth: Implications for isotopic analyses. *Archaeometry* **57**, 1104–1124 (2015).

110. D. R. Green, T. M. Smith, G. M. Green, F. B. Bidlack, P. Tafforeau, A. S. Colman, Quantitative reconstruction of seasonality from stable isotopes in teeth. *Geochim. Cosmochim. Acta* **235**, 483–504 (2018).

111. S. A. Blumenthal, T. E. Cerling, T. M. Smiley, C. E. Badgley, T. W. Plummer, Isotopic records of climate seasonality in equid teeth. *Geochim. Cosmochim. Acta* **260**, 329–348 (2019).

112. A. Zazzo, R. Bendrey, D. Vella, A. P. Moloney, F. J. Monahan, O. Schmidt, A refined sampling strategy for intra-tooth stable isotope analysis of mammalian enamel. *Geochim. Cosmochim. Acta* **84**, 1–13 (2012).

113. A. Delgado Huertas, P. Iacumin, B. Stenni, B. Sánchez Chillón, A. Longinelli, Oxygen isotope variations of phosphate in mammalian bone and tooth enamel. *Geochim. Cosmochim. Acta* **59**, 4299–4305 (1995).

114. R. D. Field, Observed and modeled controls on precipitation δ^{18}O over Europe: From local temperature to the Northern Annular Mode. *J. Geophys. Res.* **115**, D12101 (2010).

115. J. M. McArthur, R. J. Howarth, T. R. Bailey, Strontium isotope stratigraphy: LOWESS version 3: Best fit to the marine Sr-isotope curve for 0-509 Ma and accompanying look-up table for deriving numerical age. *J. Geol.* **109**, 155–170 (2001).

116. A. Kassambara, *rstatix: Pipe-Friendly Framework for Basic Statistical Tests* (2020); https://cran.r-project.org/package=rstatix.

117. H. Wickham, L. Henry, *tidyr: Tidy Messy Data* (2019); https://cran.r-project.org/package=tidyr.

118. L. Alathea, *captioner: Numbers Figures and Creates Simple Captions* (2015); https://cran.r-project.org/package=captioner.

119. D. Gohel, *flextable: Functions for Tabular Reporting* (2020); https://cran.r-project.org/package=flextable.

120. H. Wickham, *ggplot2: Elegant Graphics for Data Analysis* (Springer New York, 2016).

121. H. Wickham, *stringr: Simple, Consistent Wrappers for Common String Operations* (2019); https://cran.r-project.org/package=stringr.

122. H. Wickham, R. François, L. Henry, K. Müller, *dplyr: A Grammar of Data Manipulation* (2019); https://cran.r-project.org/package=dplyr.

123. Y. Xie, knitr: A comprehensive tool for reproducible research in R. *Implement Reprod Res.* **1**, 20 (2014).

124. D. Gohel, *officer: Manipulation of Microsoft Word and PowerPoint Documents* (2020); https://cran.r-project.org/package=officer.

125. D. Kahle, H. Wickham, ggmap: Spatial Visualization with ggplot2. *R J.* **5**, 144–161 (2013).

126. G. Daróczi, R. Tsegelskyi, *pander: An R 'Pandoc' Writer* (2018); https://cran.r-project.org/package=pander.

127. B. Auguie, *gridExtra: Miscellaneous Functions for "Grid" Graphics* (2017); https://cran.r-project.org/package=gridExtra.

128. J. Ooms, *magick: Advanced Graphics and Image-Processing in R* (2020); https://cran.r-project.org/package=magick.

129. T. L. Pedersen, *patchwork: The Composer of Plots* (2020); https://cran.r-project.org/package=patchwork.

130. A. Kassambara, *ggpubr: 'ggplot2' Based Publication Ready Plots* (2020); https://cran.r-project.org/package=ggpubr.

131. C. O. Wilke, *cowplot: Streamlined Plot Theme and Plot Annotations for 'ggplot2'* (2019); https://cran.r-project.org/package=cowplot.

132. N. Ross, *redoc: Reversible Reproducible Documents* (2019); https://github.com/noamross/redoc.

133. OpenStreetMap Contributors, Planet dump retrieved from https://planet.osm.org (2020).